Correspondence to:
L. Cocchi,
luca.cocchi@ingv.it

Seamount-Volcanic Island Transition and Evolution From Fissural to Central Activity Inferred by the Magnetic Modeling of Salina Island (Tyrrhenian Sea)

Luca Cocchi[1] , Riccardo De Ritis[1] , Daniele Casalbore[2] , Claudia Romagnoli[3] , Federico Lucchi[3] , Claudio Antonio Tranne[3] , and Guido Ventura[1]

[1]Istituto Nazionale di Geofisica e Vulcanologia, Rome, Italy, [2]Istituto di Geologia Ambientale e Geoingegneria - CNR c/o Dipartimento Scienze della Terra, Sapienza Università di Roma, Rome, Italy, [3]Dipartimento di Scienze Biologiche, Geologiche e Ambientali, University of Bologna, Bologna, Italy

Abstract Volcanic islands represent the later stage of an early submarine volcanic activity and show different morphologies reflecting the geometry of shallow plumbing systems, magma output rate, gravitational instability, and erosive phases. Two end-member morphologies may be recognized: (a) rift-like elongated edifices and 'stellate' volcanoes and (b) cone-shaped, central-type volcanoes. While the evolution from early conical shapes to stellate shapes is relatively well known, the reverse is less constrained, commonly lacking geophysical and geological data to support it. We present magnetic forward and 3-D inverse models of the volcanic island of Salina (244-15 ka; Aeolian Arc, Southern Tyrrhenian Sea) to characterize its shallow plumbing system. The detected magnetic sources are interpreted as the crystallized portions of dykes and vertical conduits. The dykes mainly characterize the offshore of Salina Island, whereas subcircular conduits are located onshore. The results show that the early, mainly submarine phases of Salina concentrated along dykes following weakness zones of tectonic significance. As the volcanism proceeded, the subaerial activity focused on two main cone-shaped stratovolcanoes (Monte Fossa delle Felci and Monte dei Porri). The intersections among dykes and the progressive loading of volcanic products during the early growth of Salina are responsible for the transition from an early fissural basaltic activity to a later, basaltic to a last, more evolved central-type volcanism. We conclude that intrusions along pre-existing tectonic structures, dyke intersections, and loading processes related to the formation of a volcanic pile regulate the morphology and structural evolution of volcanic islands from the early, submarine phase to the later subaerial activity.

1. Introduction

Volcanic edifices are characterized by a large variability in size and shape reflecting the complex interplay through time between constructive and destructive processes (Grosse et al., 2014). The study of volcano morphology can provide valuable insights into these processes and their underlying causes, that is, tectonic/structural setting, magma composition and flux, eruptive style, and climate (Thouret, 1999). In particular, constructive processes mainly depend on the size, geometry, depth of the plumbing system, and magma output rate. The plumbing systems include shallower vertical to inclined conduits (e.g., vertical dykes, inclined sheets, and sills) and deeper magma reservoirs with different aspect ratio. In this regard, central volcanoes are commonly associated to sill-like, often superimposed, magma chambers from which prevailing vertical, subcircular conduits depart reaching the surface. On the contrary, elongated, fissural edifices are generally characterized by linear, parallel to en-echelon or interconnected networks of dyke-like conduits (Gudmundsson, 1998). These two end-member shapes may be largely modified by erosional/destructive processes ranging from small scale, superficial dismantling processes to larger scale and deeper sector and flank collapses (McGuire, 2006). Insular volcanoes and seamounts are also characterized by modifications induced by marine processes. The availability of geophysical and marine geology data allows us to significantly advance our knowledge of submarine volcanoes and their associated genetic processes (Casalbore, 2018, and reference therein). The style and emplacement of volcanic eruptions is, in fact, different below or above sea level interface, and it is also strongly dependent on the water depth (Bosman et al., 2014; McClinton & White, 2015; Mitchell et al., 2008). Morphological studies also evidence a transition from conical shapes with a subcircular base to 'stellate' forms (Mitchell, 2001) reflecting the progressive

growth of seamounts and volcanic islands. The proposed interpretation for this transition is that, when sufficiently tall, volcanic edifices are easily affected by lateral collapses, with the boundary of embayment controlled by rift zones and stress redistribution at shallow depth (Carracedo, 1994). Also, the results of numerical models show that even in the absence of collapses, dykes and lateral fissures may form by stress redistribution around a cone-like volcano due to the loading of the edifice (Roman & Jaupart, 2014). However, the transition from stellate to subcircular shapes has been also observed. This transition, which is less documented and understood, has been tentatively attributed to different causes including (a) the intersection of early subparallel dykes, which favor the formation of a single, subcircular conduit (Gudmundsson, 1998; Takada, 1989; Tibaldi, 2015); (b) the reorientation of the stress within the volcano due to collapse episodes (Maccaferri et al., 2017; Ventura et al., 1999; Walter et al., 2005); (c) magma viscosity increase at the margins of dykes with subsequent flow localization (Wylie et al., 1999); and (d) the progressive melting of the country rocks around early dykes (Quareni et al., 2001). The poorly known relationships between the surface morphology of a volcano and the geometry of its shallow plumbing system are mainly related to the lack of geophysical data allowing a detailed investigation of the inner volcanic structure of the edifice and of the shallow crust. Salina Island (Aeolian Arc, Southern Tyrrhenian Sea; Figures 1 and 2) is characterized by an early fissural, mainly submerged, activity followed by the later emplacement of the two large, up to 900-m high central-type stratovolcanoes of Monte Fossa delle Felci and Monte dei Porri. With the aim to constrain the causes of this transition, we integrate the data from magnetic modeling with the available marine geology and subaerial volcanological information. We correlate the surface morphology with the structures characterizing the inner core of the island and the crust down to 3 km below sea level (bsl, hereafter). In a previous study, De Ritis et al. (2007) proposed the interpretation of a high-resolution low-altitude aeromagnetic survey of the Salina Island, providing two forward models centered and focused mainly on the on shore structures. In this work we analyze the whole data set following an integrated approach based on the inverse and direct modeling. These latter models mainly focus on the offshore sectors of the island. The inverse model proposed here provides a comprehensive 3-D picture of the magnetic sources occurring in the whole study area. We also integrated a shipborne magnetic survey covering the north eastern offshore of Salina where two seamounts occur.

The results presented here allow us to (a) obtain a coherent image of the shallow conduits and reservoirs; (b) reconstruct the geometry, depth, and size of the shallow plumbing system of the island and surrounding offshore; and (c) put constraints on the causes of the observed transition from an early, fissural-type and seamount phase of activity to a later, subaerial activity responsible for the formation of the two larger central-type stratovolcanoes. Our study puts new constraints on the relationships between the morphology and shallow structure of the plumbing systems of volcanoes and on the formation and evolution of volcanic islands since their initial submarine stage.

2. Geological Setting

Salina Island is located in the central sector of the Aeolian volcanic arc, at the northern edge of the Vulcano-Lipari-Salina volcanic belt (Figure 1a and 1b). This belt runs along the NNW-SSE trending Tindari-Letojanni right-lateral, strike-slip fault system, which represents a lithospheric step-fault delimiting, to the west, the subvertical (70–80°), northwest dipping Ionian slab (Barreca et al., 2014; Billi et al., 2006; DeAstis et al., 2003; Lanzafame & Bousquet, 1997). The slab, which subduces below the Calabrian Arc, is affected by roll-back processes responsible for the opening, in the last 2 Ma, of the Southern Tyrrhenian Sea (Doglioni, 1991; Gvirtzman & Nur, 2001; Rosenbaum & Lister, 2004; Savelli, 2000). In the Aeolian Islands, the northern branch of the Tindari-Letojanni fault system intersects the WNW-ESE striking Sisifo-Alicudi fault system, which is characterized by strike-slip and compressive movements (DeAstis et al., 2003; Figure 1b). On the surface, the Tindari-Letojanni fault system is characterized by NW-SE to N-S striking faults and by second-order NE-SW striking faults bridging the main NW-SE shear zones.

2.1. Salina Island

Salina represents the summit of a larger, mainly submarine volcanic complex rising approximately 2,000 m above the seafloor up to the maximum altitude of 962 m above sea level of Monte Fossa delle Felci (Figures 1c and 2). The island is constituted by the Monte Fossa delle Felci and Monte dei Porri cone-shaped stratovolcanoes, together with the deeply eroded and partly collapsed Pizzo di Corvo, Pizzo Capo and Monte
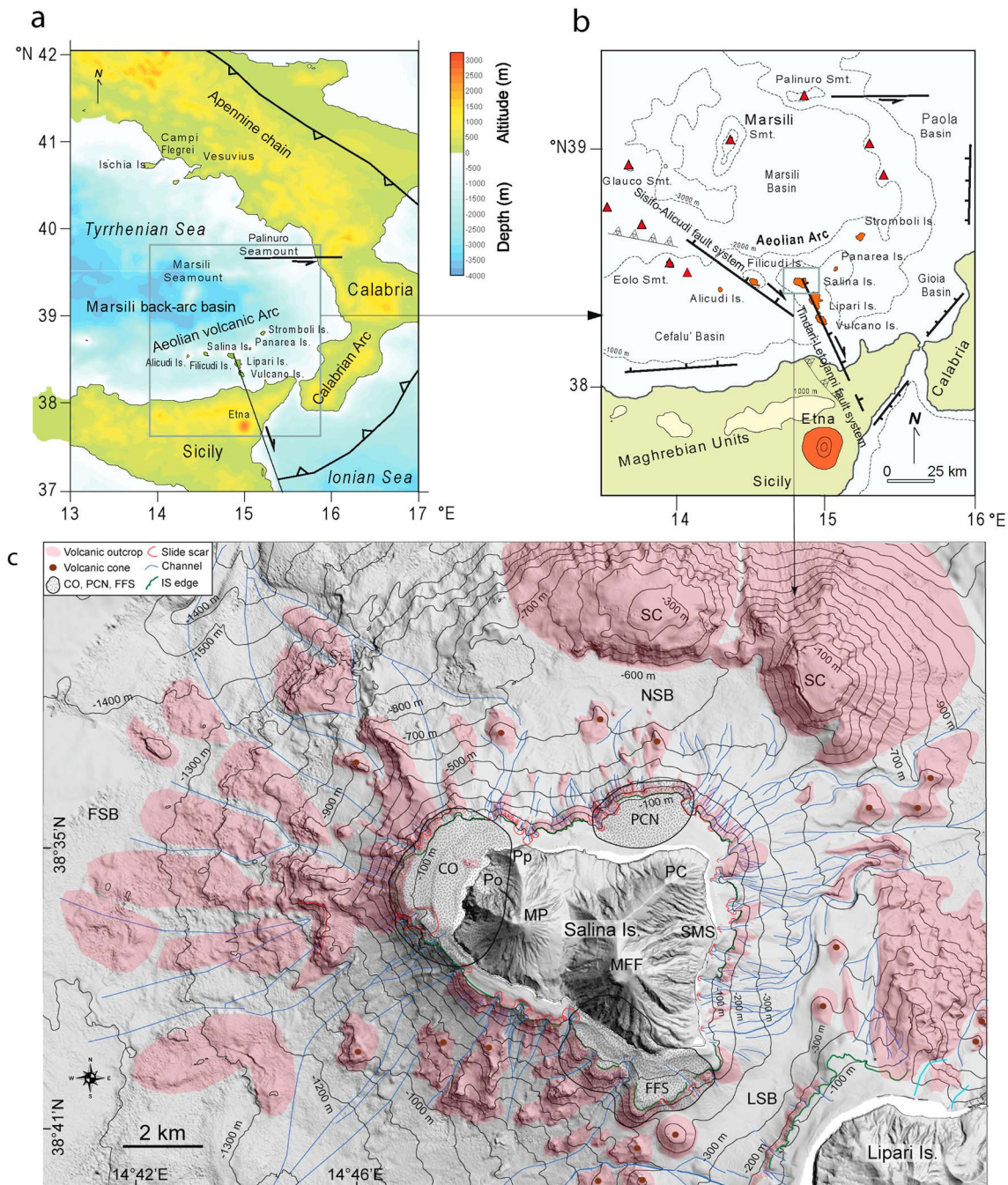
Figure 1. (a) Location and (b) structural scheme of the Aeolian Islands (modified from De Astis et al., 2003, and Barreca et al., 2014). (c) Shaded relief image of Salina Island and submarine portions with indication of main features (see text for details; modified from Romagnoli et al., 2013). MP: Monte dei Porri; MFF: Monte Fossa delle Felci; PC: Pizzo Capo; SMS: Santa Marina Salina; Po: Pollara; Pp: Punta di Perciato; CO: Pizzo di Corvo; PCN: Pizzo Capo North; FFS: Fossa delle Felci South; SC: Secca del Capo; LSB: Lipari-Salina Basin; FSB: Filicudi-Salina Basin; NSB: North Salina Basin.

Rivi volcanoes (Keller, 1980; Lucchi, Gertisser, et al., 2013). These volcanoes have mostly grown up since ~244 ka through six successive eruptive epochs (EEs) interrupted by volcanic quiescence phases and collapses, and episodes of erosion and marine terrace formation during marine oxygen isotope stages 7 and 5 (Lucchi, Gertisser, et al., 2013, Lucchi, Tranne, et al., 2013). The Salina products range in composition from early basalts to later rhyolites belonging to the calc-alkaline and HK calcalkaline magmatic suites (Lucchi, Gertisser, et al., 2013). The oldest exposed volcanic products are basaltic lava
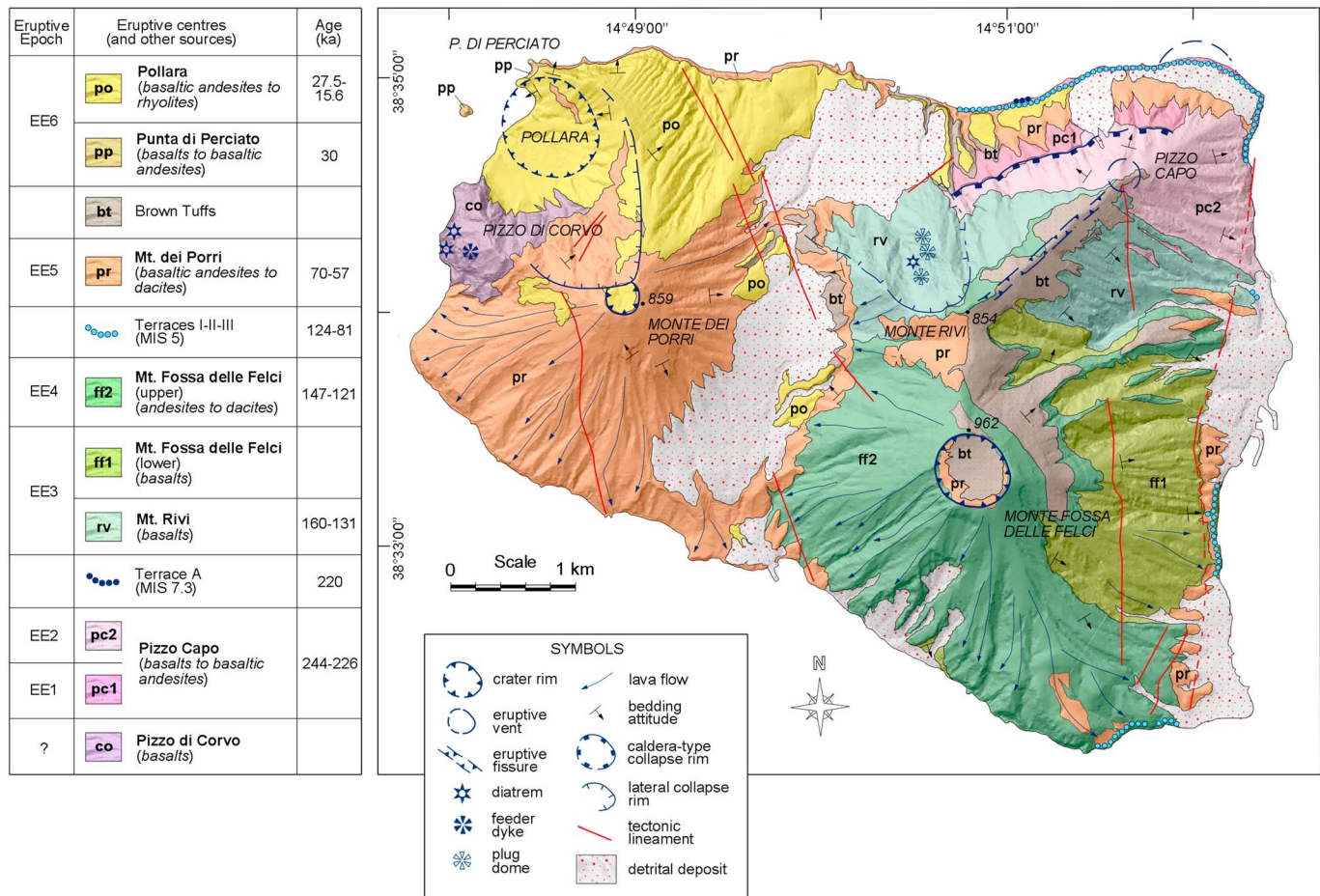
Figure 2. Schematic geological map of Salina Island (modified from Lucchi, Gertisser, et al., 2013; Lucchi, Tranne, et al., 2013).

flows and scoriae erupted by the NE-SW elongated Pizzo Capo fissural volcano (EE1-2; 244–226 ka; Figure 2), which occupies the north-eastern part of Salina Island. Its evolution was interrupted by a caldera collapse. Despite uncertain stratigraphic position and radiometric age (Lucchi, Gertisser, et al., 2013), the strongly dismantled Pizzo di Corvo stratocone in the western side of the island has been generally considered as one of the oldest volcanic centers of Salina (Figure 2; Gertisser & Keller, 2000; Keller, 1980), as also suggested by Romagnoli et al. (2018) on the basis of the characteristics of the insular shelf. Most of the central-southern sector of the island was then constructed by the basaltic to dacitic pyroclastic successions and lava flows of the twin Monte Rivi and Monte Fossa delle Felci stratocones (EE3–4, 160–121 ka). The northern portion of Monte Rivi was truncated by a N dipping sector collapse that exposed the inner portion, which is mainly made by intersecting plug domes, breccia pipes, and dykes. Volcanic activity younger than the Last Interglacial is witnessed by the basaltic-andesitic to andesitic lava flows and scoriae of the Monte dei Porri stratovolcano (EE5, 70–57 ka), occupying the western sector of Salina (Figure 2). The Monte dei Porri activity was interrupted by a NW dipping lateral collapse truncating the northwestern flank of the volcano. Along the northern rim of this collapse, the Pollara crater (EE6) produced the andesitic Punta di Perciato lava flows (30 ka) and widespread rhyolitic pumiceous successions related to two subplinian eruptions occurred at 27.5 and 15.6 ka, representing the latest eruptive episodes on Salina (Figure 2).

The few faults outcropping on the island show strikes ranging from NW-SE to N-S and dip >45°. The faults affect Monte dei Porri and the eastern sector of Monte Fossa delle Felci. The strikes of the Salina faults are consistent with the faults affecting the island of Lipari and Vulcano, likely representing the surface expression of the Tindari-Letojanni lithospheric shear zone.

2.2. Offshore Salina

The presence of (mostly) submerged volcanic edifices (Pizzo di Corvo, Pizzo Capo North, and Fossa delle Felci South) predating the oldest subaerial products exposed on Salina is suggested by the occurrence in shallow-water of submerged shelves having large widths (1,700–2,000 m) and deep erosive edges (down to 226 m bsl), which have subsided after their formation (Figure 1c; Romagnoli et al., 2018). The largest and deepest shelf is recognized around Pizzo di Corvo (Figure 1c), which is thus related to an early stage of evolution of Salina. Narrower shelves with edges at 120-127 m bsl, likely formed during the Last Glacial Maximum, are present mostly along the south-western, northern, and eastern sectors of the island (Romagnoli et al., 2018).

Below the edge of the insular shelves, the submarine flanks of Salina are steep (slope values up to 35°) and with a rough morphology due to the presence of volcanic and erosive-depositional features, mostly with radial distribution (Figure 1c; Casalbore et al., 2016). On the western submarine flanks of Salina, two main volcanic morphologies consisting of pseudo-radial linear ridges with lobate culminations are recognizable down to 1,000 m water depth. These ridges depart from the NE (offshore Pollara crater) and SW (offshore Pizzo di Corvo volcano) edge of the insular shelf, likely representing remnants of lava flows or exhumed radial dykes (Romagnoli et al., 2013). Another N-S elongated ridge extends between depths of about 300 and 700 m in the southern offshore sector of the Monte dei Porri edifice (Figure 1c). The other submarine flanks of Salina are mainly marked by a degraded morphology due to posteruptive erosive-depositional processes. Scattered, small volcanic cones are observed at various depths, especially on the southern and eastern submarine flanks of the island, where they are part of a larger volcanic belt flanking the western side of the Lipari-Vulcano-Salina volcanic alignment, likely related to an earlier stage of volcanic activity in the Central Aeolian sector (Romagnoli et al., 1989). These scattered volcanic cones and ridges are partly emplaced along NNW-SSE and NE-SW tectonic lineaments (Gamberi et al., 1997; Romagnoli, 2013).

On the whole, the submarine portions of the Salina edifice are substantially larger than the island. The base of the Salina edifice is located at depths ranging between 650 and 1,300 m bsl, apart for the southeastern sector, where a saddle at about 300 m connects Salina to Lipari (Lipari-Salina Basin, LSB in Figure 1c; Casalbore et al., 2016; Romagnoli et al., 2013). To the west, a saddle at about 1,370 m bsl separates Salina from the Filicudi volcanic complex (Salina-Filicudi Basin, SFB in Figure 1c; see also Calanchi et al., 1995). To the north and northeast of Salina, a small basin (North Salina Basin, NSB in Figure 1c) is delimited by the two seamounts of Secca del Capo (SC in Figure 1c), rising to depths of 250 m (the western one) and 27 m (the eastern). Both seamounts are flat-topped and homogeneously draped by sediments (Gamberi et al., 1997) attesting the end of the volcanic activity and wave reworking during sea level fluctuations. In detail, the eastern seamount shows a flat, eroded summit down to 100 m bsl, with a NNW-SSE direction of elongation. Samples dredged from the summit of Secca del Capo indicate a calc-alkaline andesitic composition (Romagnoli et al., 1989).

3. Data and Methods

3.1. Data Acquisition

Magnetic data for Salina Island were acquired during two aeromagnetic campaigns carried out in October 2003 and December 2005 (De Ritis et al., 2007). Both surveys were flown along NE-SW oriented lines at constant altitude of about 500 m over the sea and with constant terrain clearance of about 200 m (drape mode) over the island. The line spacing is 1,500 m (Figure 2a) for both surveys. The lines of the second fly are in between those of the first one. The data sets are merged to increase the survey resolution with a line spacing of about 750 m.

In order to get the crustal magnetic anomaly field, each data set was processed to remove the daily variations and the main field components and then reduced at the same geomagnetic epoch (International De Ritis et al., 2007). The data were gridded using the minimum curvature algorithm with a cell size of 200 m to obtain the Total Magnetic Intensity field map (hereafter TMI). The gridded data were also microleveled to remove the residual small-scale errors in the data sets (Ferraccioli et al., 1998). The longer wavelength components of the field caused by sources placed outside the study area were also high-pass filtered (15 km).
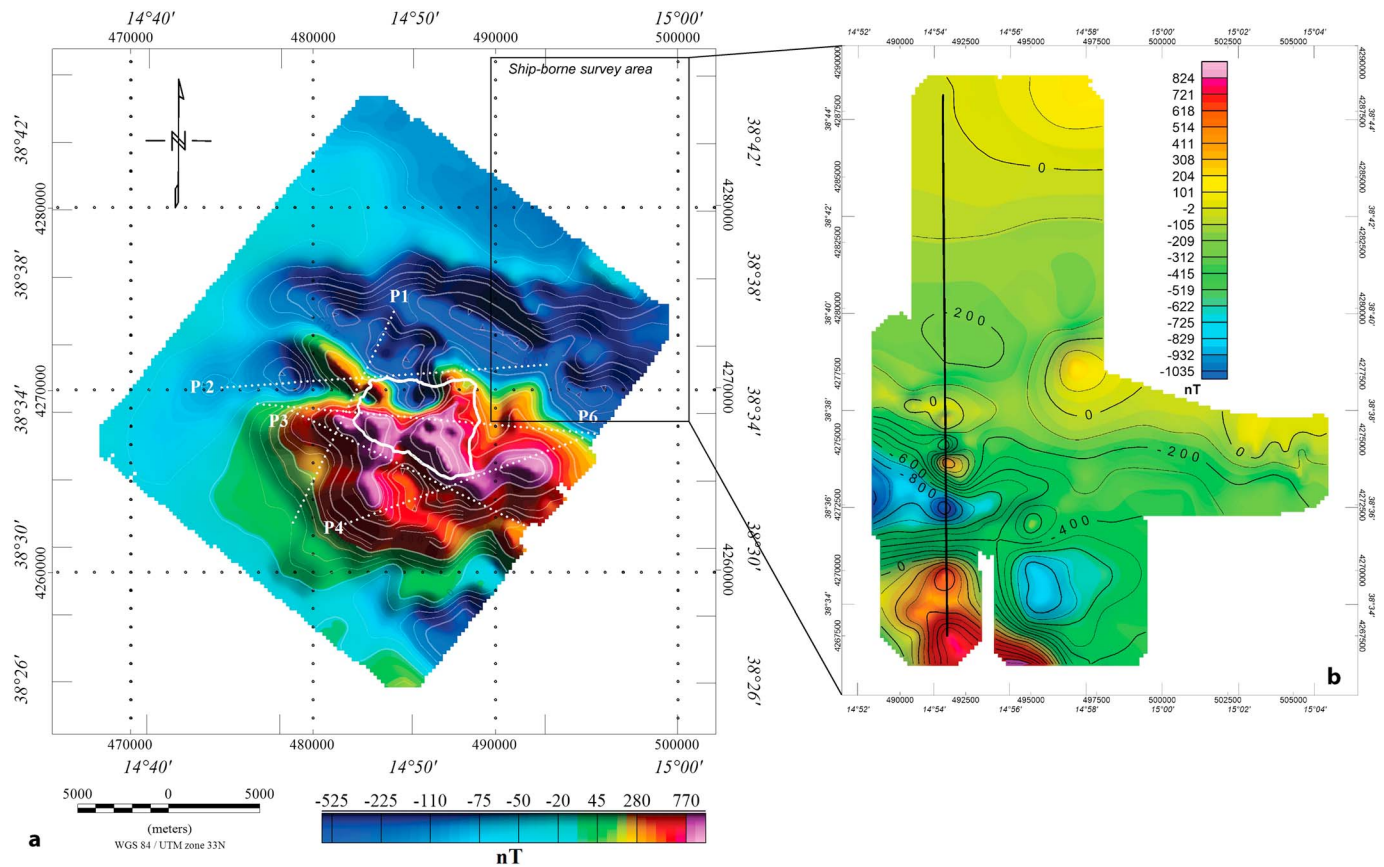
AGU
100
ADVANCING EARTH
AND SPACE SCIENCE

Journal of Geophysical Research: Solid Earth

10.1029/2018JB017113

Figure 3. (a) Aeromagnetic anomaly map of Salina Island and surrounding offshore areas. Forward modeling profile tracks (P1-6) are reported in white dotted line. Outline of Salina Island is the thick white contour. (b) Ship-borne magnetic anomaly map of Secca del Capo offshore region; track profile P5 is reported in black line

A further data set was employed to model the NE Salina offshore areas in correspondence of Secca del Capo (seamounts SC in Figure 1c). This data set derives from a shipborne acquisition performed in 2013 by the R/V Urania oceanographic vessel (Dialti et al., 2013).

The overall TMI of Salina Island and surrounding areas (Figure 3) shows an overall dipolar pattern generated by singular and composite anomalies. All these anomalies are directly magnetized along the present day inducing field directions or very close to them (I=54°, D= 2° from International Geomagnetic Reference Field, IGRF).

3.2. Magnetic Modeling

The main aim of magnetic surveying is to get qualitative and quantitative information about the causative sources and to interpret them on the base of the geological knowledge of the area. In this work, we use both inverse and direct approaches as complementary methods.

The first method is aimed to get the overall 3-D smooth distribution of the magnetic sources with a resolution directly related to the mesh cell size. We consider a smooth inversion appropriate for the Salina Island data set because of its complex source layout. This complexity derives from the occurrence of several sources lying close together, both onshore and offshore. As a consequence, the source magnetic effects overlap and clear boundaries between them cannot be separated. The second method, based on the constraints derived by the inverse model (e.g., susceptibility values, shape, depths, and horizontal extent of the bodies), works on 2.75-D forward model, which allows to reconstruct the geometry and susceptibility values of crustal bodies along and across the profile track. This interpretative method is aimed to (a) better represent the along section geometry of each source, (b) identify the shallower to outcropping sources, and (c) add volcanic and structural constraints to the modeling.

As a result, using both 3-D smooth and 2.75-D modeling, we provide a complete interpretation of the Salina anomaly field. However, this approach does not fully remove the intrinsic ambiguity of the potential fields, and our modeling is aimed to interpret as best as possible the main magnetic sources related to the volcanic and structural features.

In volcanic areas, intense magnetic anomalies occur because of the high magnetization of the rocks. Paleomagnetic data and susceptibility measurements provide a precise estimate of the surficial magnetic properties (induced and remanent magnetizations), which have to be considered as general reference to constrain the magnetic modeling. A few susceptibility and remanent magnetization measurements on the Salina volcanic rocks are reported in Barberi et al. (1994) and De Ritis et al. (2007), but they lack the inclination and declination angular values. In addition, the paleomagnetic studies of Zanella (1995) have highlighted that magnetic declination and inclination of the andesitic lava flows of the Mt. dei Porri and Fossa delle Felci volcanoes have an average value of -5 and 51.4°, respectively. These latter values are close to the declination and inclination values of the present-day Earth magnetic field (D=2°, I=54°; IGRF 2003). The above mentioned data indicate that the Koenigsberger ratio ranges from 1 to 5, so highlighting the dominance of the remanent on induction. In order to have an idea of the magnetic properties of the study area, we also considered the Vulcano Island data reported in Lanza and Zanella (2003) and Blanco-Montenegro et al. (2007). This island, together with Lipari and Salina, belongs to the same volcanic ridge, and its subaerial primordial phase (135 ka) have a time span overlapping 90% of the Salina volcanic products (<130 ka), while the oldest, volumetrically reduced, Salina volcanic products is about 220 ka (see Figure 2). More in general, all the Salina-Lipari-Vulcano volcanic ridge ages are well inside the Brunhes chron (0.8 ka) implying the sole existence of normal polarities during the ridge construction stages. Therefore, the secular variation effects of the geomagnetic field at Salina are expected to be averaged on the remanent magnetization directions. The Vulcano mean paleomagnetic directions are D=9.4°, I=53.2° (Lanza & Zanella, 2003). This direction differs from the geocentric axial dipole direction (D=0°, I=57.8°), most likely because of the longterm, non-axial-dipolar magnetic field component (Blanco-Montenegro et al., 2007). Considering the above cited paleomagnetic data of Mt. dei Porri and Fossa delle Felci volcanoes, this condition probably holds also for the whole Salina Island. As a consequence, the bulk magnetization direction at Salina is almost parallel to the axial dipole field, which, in turn, is close (<10°) to the used IGRF magnetic angular values. In the inversion algorithms Maginv3D and UBC-Mag3D (Li & Oldenburg, 2003) is not a problem if the remanent component is close to the direction of the induced field. Consequently, the obtained susceptibility distribution from the inversion is reasonably reliable (Paine et al., 2001).

3.2.1. Inverse modeling

Inverse modeling was carried out for susceptibility using a variation of the Li and Oldenburg's (2003) smooth inversion method, which considers prismatic cells fitting the topographic surface (MGinv3D, 2013, http://www.scicomap.com/MGinv3D.html). This 3-D voxel inversion code also uses the algorithm by Zhu et al. (1994) to perform the smoothness-constrained minimization of the data misfit (see Figure 4). The crustal volume lying below the surface is represented by a core model mesh with $300 \times 300 \times 200$ m^3 prismatic cells in the x, y, and z direction, respectively. The model bottom was fixed at 7-km depth, while all the mesh was expanded using padding cells with increasing dimension going outward in the three axial directions (total number of the model cell is $79 \times 87 \times 42$). The TMI field was sampled at the center of each cell and the target misfit set to be variable for the resulting 5,021 observation points of the model. The mesh bottom has been chosen on the basis of the local stratigraphic sequence, which consists of volcanic and sedimentary units overlying the Calabrian Arc crystalline rocks; these latter are generally considered not or very low magnetic (Barberi et al., 1994). Therefore, the depth to the bedrock represents the thickness where the magnetic sources most likely lie between 3 and 7 km (DeAstis et al., 2003, and references therein). Also, the depth of the magmatic reservoirs related to the more recent (24 and 13 ka) eruptions on Salina is below 7–8 km (De Ritis et al., 2013).

We obtained different models with a rather similar geometry by varying parameters, such as the misfit/smoothness trade-off and the alpha parameters (Li & Oldenburg, 1996). Among the achieved solutions, we select the model best fitting the geological and volcanological information and with the lower difference between the observed and predicted data (Figure 4). The model smoothness weights in the x, y, and z directions were set to the unit, and we carried out an unconstrained inversion (without initial or reference model) obtaining the data fit to root-mean-square (RMS) data misfit of 1.29 after 300 iterations. The RMS
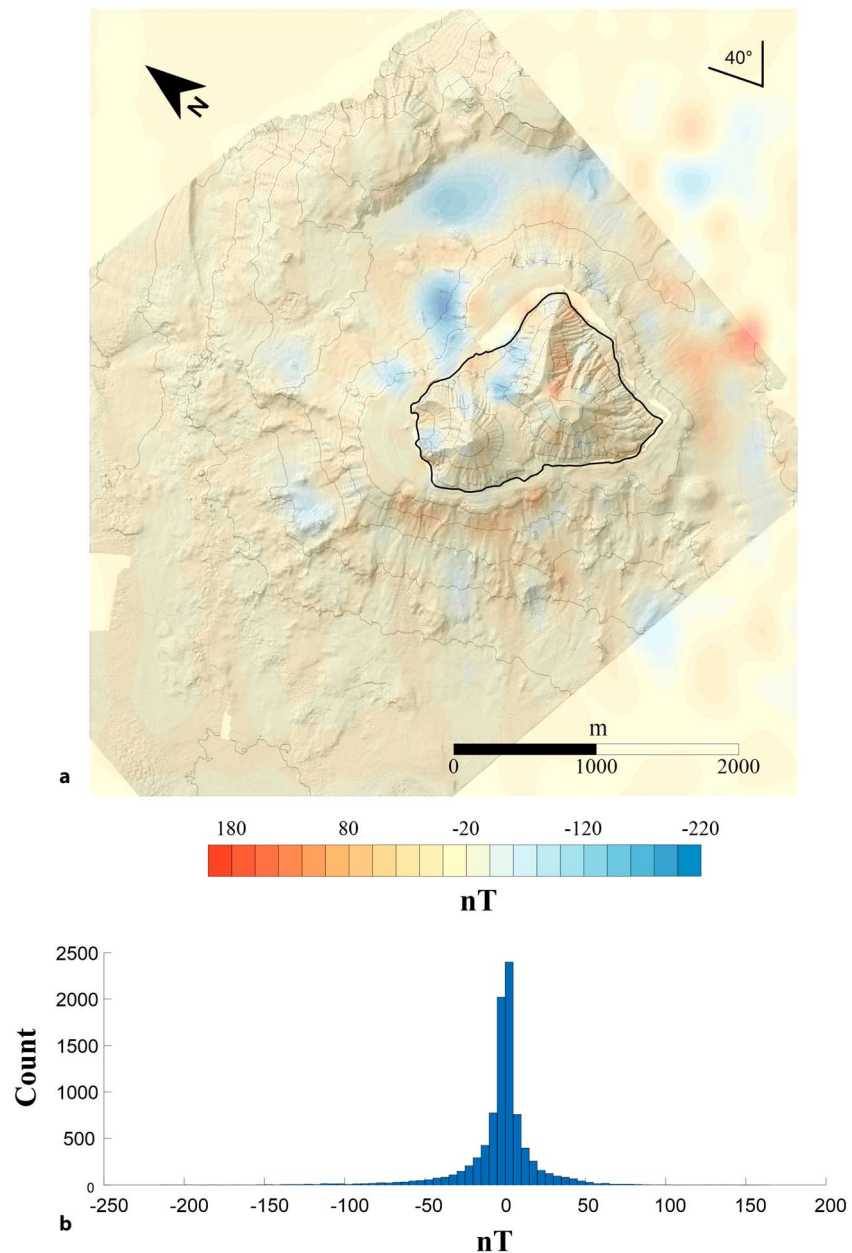
Figure 4. (a) 2-D distribution of error values between observed and predicted magnetic anomaly fields overlaid on the digital elevation model of Salina region. Outline of Salina Island is the thick black contour. Histogram of the error values (subpanel b) shows a Gaussian normal distribution.

misfit is defined by predicted minus the observed data divided by the target misfit (Li & Oldenburg, 1996). The value of 1.29 means that inverse algorithm fitted the data to 1.29 times the target error on an RMS basis. This suggests that inversion procedure provides a fairly good reconstruction of the observed data.

The large values shown in Figure 4 highlight that the error extremes can be larger, while the overall RMS misfit can be quite reasonable. This is important because it demonstrates that the errors in the data, which are more than just the measurement errors, can be accommodated by the inversion process and thus ignored because of the goodness the overall data fitting. The inverse model is shown in Figure 5 as 0.06 SI isosurface representing the susceptibility limit, encompassing most of the sources volume with meaningful magnetic properties. This susceptibility value corresponds to an induced magnetization (Ji) of about 2 A/m, considering the inducing field (Inclination 54° and declination 2°) of the area at the time of the surveys (IGRF 2003).
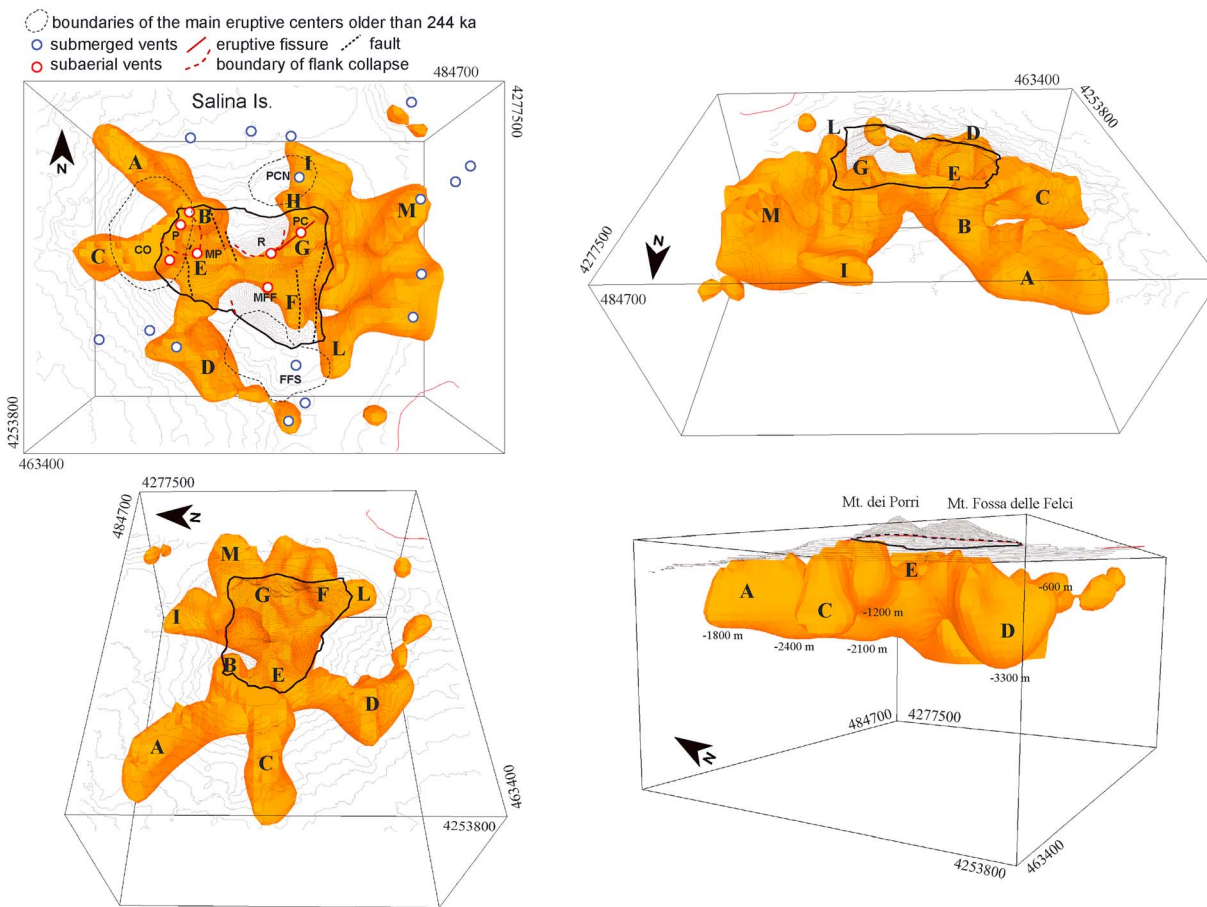
Figure 5. Inversion modeling results described by the 0.06 SI isosurface encompassing most of the source rock volume with meaningful magnetic properties. The magnetic sources are labeled with letters. The panels sequence shows the vertical view, the south, eastern, and southwestern perspectives, respectively. The digital elevation model contouring, the main vents, and volcano-tectonic structures are also reported in solid light line (from Figures 1c and 2). The acronyms of the volcano names are also reported (see Figure 1c for the legend). The depth to the base of the 0.06 isosurface is reported in the last panel.

All the sources shown in Figure 5 (indicated by letters) have a susceptibility of 0.92 SI (Ji=3.22 A/m) on average, with the largest value of 0.132 SI (Ji=4.6 A/m) in the easternmost sources (see also Figure 3). Therefore, the depicted model represents the rough core source shape of the TMI field causative bodies. In order to make a comparison between the two modeling approaches, 2-D sections are extracted from the 3-D voxel model of Figure 5 along the tracks selected for the forward modeling (Figure 3) and described in the next section.

3.2.2. Forward Modeling

The forward computation is carried out using the GmSYS tool of Oasis Montaj by Geosoft (based on Won & Bevis, 1987) along six profiles extracted from the TMI gridded data (traces in Figure 3). These profiles aim to better solve the high-frequency content of the magnetic anomaly field and to constrain our models with geo-structural information derived from field and marine geology data (Figures 1c and 2). The fitting is obtained by manually varying the geometry and susceptibility of the sources. In addition, the 2.75-D forward model technique takes into account the model parameter variations along and across-strike direction. The 3-D inversion model provides constrains on the overall smooth geometries, the depth of the sources, and the susceptibility range of the sources and background. The Earth's magnetic field intensity, inclination, and declination used in the modeling derive by the IGRF 2003 model.

We also constrained the model susceptibilities using the values measured on the Salina Island lithologies (De Ritis et al., 2007). As a consequence, the highly magnetic bodies were set at 0.14/0.15 SI (5/5.3 A/m), a value fully compatible with that obtained by the 3-D inversion approach for the same positions and depths. The susceptibility background was interpreted as related to the low - to not magnetic sequence of the

sedimentary and crystalline units of the Calabrian Arc and of the volcanoclastic deposits (0 SI up to 0.03 SI; De Ritis et al., 2007, and reference therein). Considering the extension, position, and spectral content of the field of the profiles, we fix the bottom of the model at about 2.5 km bsl. Variation of susceptibility for depths >2.5 km does not change substantially the computed magnetic profiles.

4. Results

The magnetic data of Figure 3 show a complex pattern composed by several, overlapping high-intensity anomalies mostly lying in the eastern, southern, and western offshore areas. The western area shows a more simple pattern if compared to the eastern one. This is mostly related to a less complex distribution of the causative sources in the western area. On the contrary, the number of convoluted magnetic anomalies increases to the east; this reflects a more complex overlap of the sources. As a consequence, the western part of the inverse model (Figure 5) is somewhat better solved by the algorithm and we can consider a larger level of confidence about the geometries and depths of the sources lying in this side of Salina. Figure 4 reports the overall error (predicted minus observed data) having a 370-nT maximum variation range (from -163 to 220 nT), representing ~20% of the intensity range of the TMI field of Figure 3. The large error range represented in Figure 4a is mostly restricted in local areas lying in the eastern part of the study area (e.g., the saddle between Mt. dei Porri and Fossa delle Felci-Rivi). As reported above, these are relatively complex sectors where more coalescing sources occur. Conversely, the remaining part of the error map is characterized by a range of about 145 nT, roughly 7% of the observed magnetic intensity range (Figure 3). Nevertheless, no clear trends are evident in Figure 4a suggesting a random distribution of the errors (Figure 4b).

The comparison between the new inverse and direct modeling (susceptibility) and the direct modeling of De Ritis et al. (2007; total magnetization) has been carried out considering that in the weak terrestrial magnetic field (~43,982.0 nT, IGRF model), the intensity of the induced magnetization can be derived by the susceptibility measurements (Hinze, et al., 2013). As above mentioned, the induced and remanent magnetization angular values are similar and their intensity can be considered, in a first approximation, additive along the direction of the Earth's magnetic field. Therefore, the induced magnetization deriving from the susceptibility values obtained by our inverse and direct models could be considered equivalent to the total magnetization derived from the modeling carried out in De Ritis et al. (2007).

4.1. Inverse Modeling

High-intensity magnetic features (B, G, E, and F in Figure 5) occur in correspondence of the four major volcanic structures on shore Salina (Pollara, Pizzo Capo, Monte dei Porri, and Monte Fossa delle Felci, respectively). In the western Salina offshore, the model shows a pseudo-radial arrangement of the sources, characterized by three arms departing from the island and going outward in NW-SE, E-W, and N-S directions, respectively (sources A, C, and D in Figure 5). Source A lies in the marine sector offshore the NW corner of the island (Figure 5) and clearly overlaps the NW-SE morphological ridge lying offshore the island (Figure 1c). Both the magnetic source and the morphological ridge are about 4 km long. Source A has a subvertical attitude, roughly extending from a depth of 600 m down to 1,800 m bsl, and enlarging close the island, near the source B (Figure 5). This latter lies just north of the Pollara crater, in correspondence of the inferred vent of the Punta di Perciato lava flow (Lucchi, Gertisser, et al., 2013). Source B geometry depicts a subvertical cylinder extending from the topography down to 1,000-m depth, where it coalesces with the source A (Figure 5).

Source C (Figure 5) departs from the Pizzo di Corvo volcano remnants and extends westward (Figure 2). Also, this source, similarly to source A, overlaps a submarine morphological ridge placed along the Salina western submarine flank, and extending over 1,000 m of water depth (Figure 1c). This source is 3 km elongated in the E-W direction and reaches a depth of about 2.4 km bsl (Figure 5). The shallower part of source C lies in correspondence of the remnants of the largely dismantled Pizzo di Corvo volcano, where a wide, subrounded insular shelf with maximum shelf edge depth at -226 m is present (Figure 1c and 2; Romagnoli et al., 2018).

Source D is placed in the southern Salina offshore and is characterized by a southward deepening upper surface (Figure 5). In its more external and deeper extension this source strikes NW-SE and reaches a depth of 3,300 m bsl, overlapping an area characterized by several volcanic features (possibly lava flows and small

cones) to the south of Monte dei Porri (Figure 1c). Moving onshore, source D becomes shallower and changes to a N-S strike in proximity of the Monte dei Porri volcano. The narrow, conduit-shaped, source E is placed below the Monte dei Porri structure, lying a few hundred meters below the topography, down to the depth of 1,800 m bsl. This source is placed at the intersection of sources A-B-C-D.

In the Salina onshore and offshore eastern sectors the magnetic anomaly field is more complex to decipher because of the close proximity of the magnetic sources (F, G, H, I, L, and M in Figure 5). The inverse model is not able to solve each anomaly separately (particularly the low frequencies). As a consequence, the obtained bodies coalesce at depth, although they most likely belong to distinct sources. Nevertheless, we consider that the model has properly depicted the rough and general geometry of this ensemble of sources, especially in its shallower part. The sources lying in the eastern sector are generally deeper than those of the western one.

Sources G, F, and H are located in correspondence of the emerged portions of the eastern Salina edifices and their nearest offshore. Source G is located just below the Pizzo Capo volcanic structure (Figure 2) and follows its NE-SW strike. The upper surface of this source reaches the top eruptive fissure of Pizzo Capo, while its depth cannot be determined (Figure 5). Source F lies beneath the central sector and southeastern flank of the Monte Fossa delle Felci volcanic edifice (Figure 2). This source roughly follows a NW-SE direction and, as for source G, its depth to the bottom is not defined. Source H has a subvertical and cylindrical shape, extending down to the 600 m depth (Figure 5); it stands near to the northeastern coast of Salina Island, in correspondence of a wide, semicircular insular shelf that has been interpreted as the eroded remnant of the early Pizzo Capo North volcanic center located off the northern coast of Salina (Figure 1c; De Ritis et al., 2007; Romagnoli et al., 2018). This source partly overlaps source I, located about 1.5 km north of the island. This latter source strikes NW-SE, extends down to the 1,000 m depth, and reaches the offshore volcanic outcrops lying in the lower flank of the island (Figure 1c).

The N-S elongated source L lies at the southeastern edge of the island, in correspondence of a wide and deep (edge at 210 m depth) insular shelf located offshore the southern flank of Monte Fossa delle Felci (Figure 1c). Some volcanic features occur in this area: (a) the eroded remnant of the Fossa delle Felci South small volcanic centers, formed in the early volcanic stages of Salina (Romagnoli et al., 2018), and (b) some small isolated volcanic cones southward from the shelf area (Figure 1c).

At the easternmost side of the model, source M develops in the submarine sector offshore Salina, placed no more than 2 km far from the island. In this part of the model the inversion solution is not well defined, and source M (and a north-eastward extension of source L) coalesces in a single deeper body (Figure 5). In particular, source M appears NE-SW elongated and extends 1,400 m below the seafloor, while source L extension follows a poorly defined NE-SW strike. In this area, the magnetic field is most likely influenced by the existence of a widespread submarine volcanic outcrop area (with volcanic cones and ridges) extending from the northern offshore of Lipari to Secca del Capo (Figure 1c).

4.2. Forward Modeling

Forward modeling of the western sector offshore Salina Island is reported in cross section P1 (Figure 6; see location in Figure 3). The 2.75-D model clearly shows two main magnetic bodies (SI 0.11/0.12/0.14) having thickness of about 1,300-1,500 m and likely representing sources A and C, as clearly shown in the cross section (see upper panel of Figure 6) extracted from the inverse model of Figure 5. These two main bodies are placed on an intermediate-susceptibility (SI 0.05–0.066) rock sequence interpreted, according to the available geochemical data (Lucchi, Gertisser, et al., 2013; Lucchi, Tranne, et al., 2013), as related to the more evolved volcanic products forming the western flank of Salina.

Cross section P2 (Figure 7) is a forward model of the northern portion of the island. From west to east, we observe a thin sequence of highly magnetized rocks interpreted as lava flows (0.12–0.13 SI) partly interbedded to a shallow, poorly magnetized lithology. In the middle of the section we note two large highly magnetized blocks interpreted to correspond to sources A and I already identified in Figure 5. These two bodies are separated by a lower magnetized sequence possibly consisting of reworked/chaotic deposits derived from the erosion and partial collapse of the north flank of Monte Rivi.

The southern side of the Salina offshore is characterized by the N-S trending magnetic D that appears well modeled in profile P3 (Figure 8). This block shows an irregular shape in depth probably due to the coalescence of two or more sources. The southeastern sector of Salina is characterized by a 1- to 1.5-km-thick
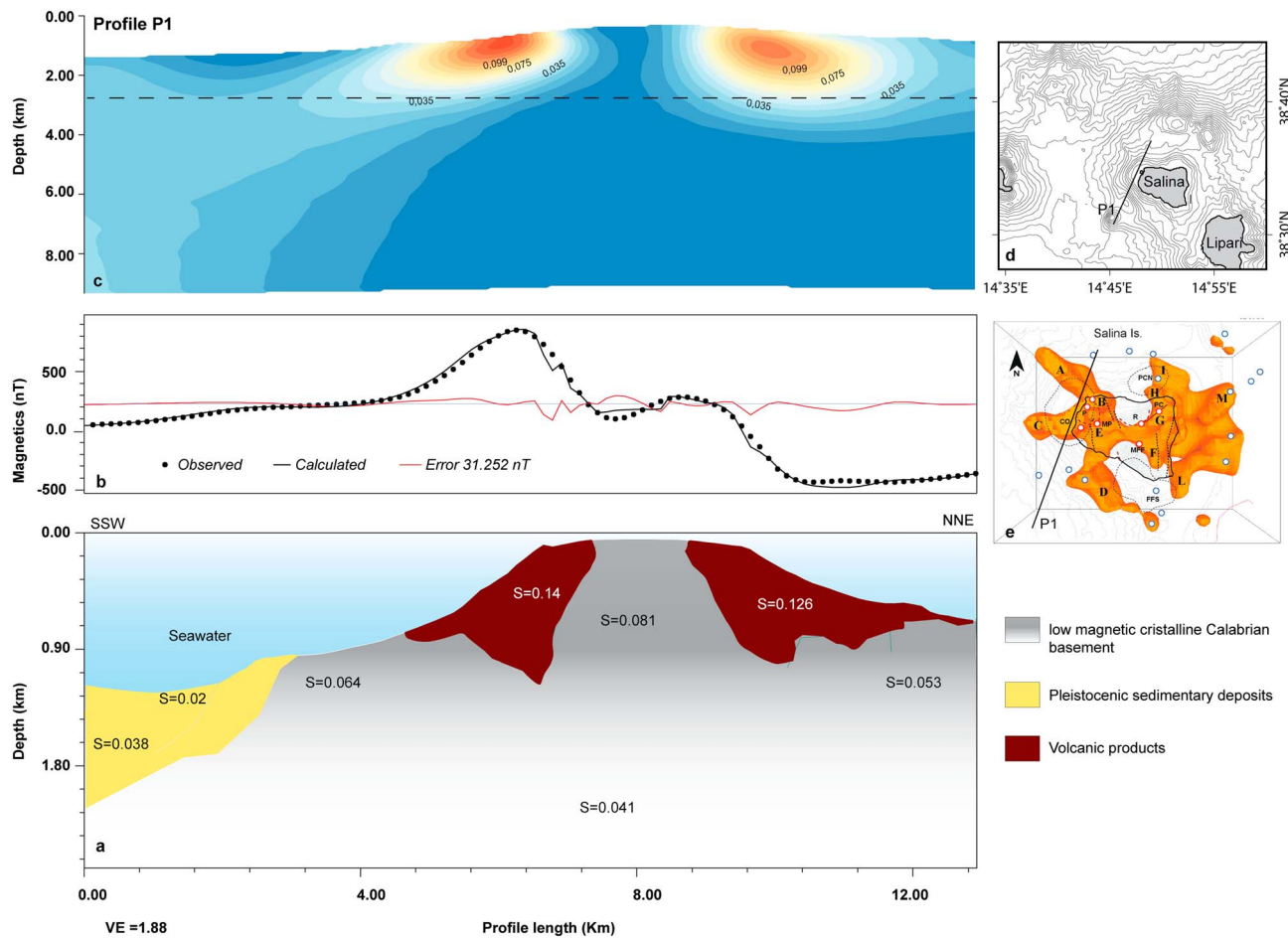
Figure 6. SSW-NNE 2.75-D forward magnetic model of western offshore area of Salina Island (track of profile P1 in the insets on subpanel d); (a) distribution of magnetized causative bodies obtained by best fit between observed and computed magnetic anomaly profiles (subpanel b). (c) X-Z cross section extracted from 3-D inverse model (Figure 5); the dashed line identifies the depth extension of forward model. The top view of the 3-D inversion of Figure 5.

rock sequence having low susceptibility values possibly reflecting the dacitic compositions of the volcanic products from Monte Fossa delle Felci. This setting is described in the cross section P4 (Figure 9), where we also observe a highly magnetized body placed northeastward of the Salina coast. This corresponds to source M in Figure 5 and can represent a subintrusive body having deep roots probably related to the northward extension of the Lipari offshore volcanic centers (Figure 1c). The cross section from the 3-D inverse model highlights how this large source deepens in a NE direction up to 4 km of depth (Figure 9).

In order to evaluate the magnetic anomaly pattern of surrounding areas, we performed a 2.75-D model along the profile P5, which intercepts the Secca del Capo seamounts area (Figures 1c, 3 and 10). The P5 profile crosses the seamount and shows a low susceptibility body (0.03–0.07 SI) at the top of the edifice, which is consistent with the occurrence of hydrothermally altered deposits as previously proposed by Gamberi et al. (1997) and Panieri et al. (2005). Active or past hydrothermal processes could be responsible for the magnetic properties drop in the interested rock volume because of (a) the high temperatures (T> Curie temperature) determined by the circulating hydrothermal fluids and (b) the alteration processes caused by hydrothermalism. These latter processes can modify the magnetite and titanomagnetite content of the rocks, for example, by magnetite (ferromagnetic) to pyrite (paramagnetic) transformation (Ade-Hall et al., 1971; Novosel et al., 2005; Rona, 1978; Szitkar et al., 2015).

Profile P6 (Figure 11) highlights the prevailing E-W distribution of the internal crustal features of Salina Island. The forward model identifies a main crustal basement showing low magnetization (0.03 SI). The main island bedrock is characterized by a mildly to highly magnetic susceptibility lithology (0.08–0.1 SI), which ranges with an uneven thickness between 200- to 2,000-m depth. This layer is covered by a high
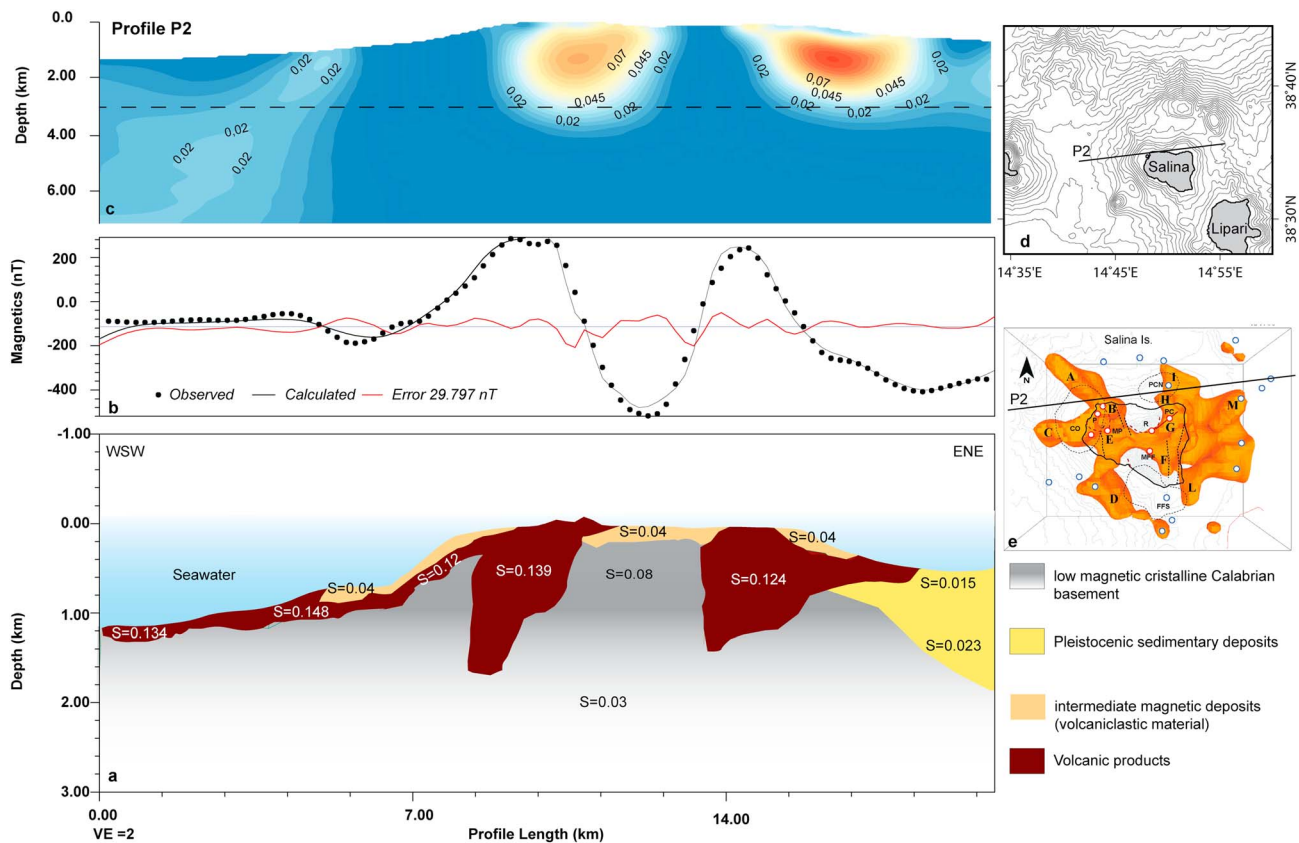
Figure 7. WSW-ENE 2.75-D forward magnetic model of northern off shore area of Salina Island (track of profile P2 in the insets on subpanel d); (a) distribution of magnetized causative bodies obtained by best fit between observed and computed magnetic anomaly profiles (subpanel b). (c) *X-Z* cross section extracted from 3-D inverse model (Figure 5); the dashed line identifies the depth extension of forward model. The top view of the 3-D inversion of Figure 5.

magnetic sequence interpreted as related to lava flows, which represent the dominant lithology of the Monte dei Porri and Fossa delle Felci volcanoes. The effusive products show a maximum thickness of 1 km in the western side of the island, in contrast to the thinner deposits observed on the eastern side. The 3-D inverse cross section points out the inner distribution of about 1- to 3-km-deep magnetic sources connected to the main volcanic centers. From west to east we can distinguish the causative sources related to the lava sequence offshore the Pizzo di Corvo and Monte dei Porri edifices, and the Monte Fossa delle Felci cone, and the eastward large volcanic roots related to the northern extension of the Lipari offshore volcanism (source M in Figure 5, location in Figure 1c).

5. Discussion

The results of the magnetic modeling of Salina show that the subsurface structure of the island consists of high magnetic bodies extending from the topography-bathymetry interface to a maximum depth of about 3,000 m bsl (Figures 5–11). The shallower bodies mainly occur below or around the main on-land volcanic edifices (Monte dei Porri, Monte Fossa delle Felci, Pizzo Capo, and Pizzo di Corvo) and the older, submerged centers and dyke-like bodies located around the island (Figures 1c and 5). We interpret the up to 3,000 m deep sources as the shallower portions of the crystallized shallow plumbing systems of the eruptive centers. The shape of the shallower sources is consistent with a sheet-like geometry suggesting the occurrence of lava flows (e.g., Figures 7 and 11). The deeper sources of Salina occur in the western and eastern offshore of the island (Figure 5). In the western offshore, two linear magnetic features extend westward, offshore the Monte dei Porri-Pollara area (Figure 1c, A and C in Figure 5). These two sources are located in correspondence of two morphological ridges extending in depth from about 300 to 800 m bsl (Figures 1c and 5). We propose that these ridges and the corresponding deep magnetic sources represent dykes belonging to the early, submarine
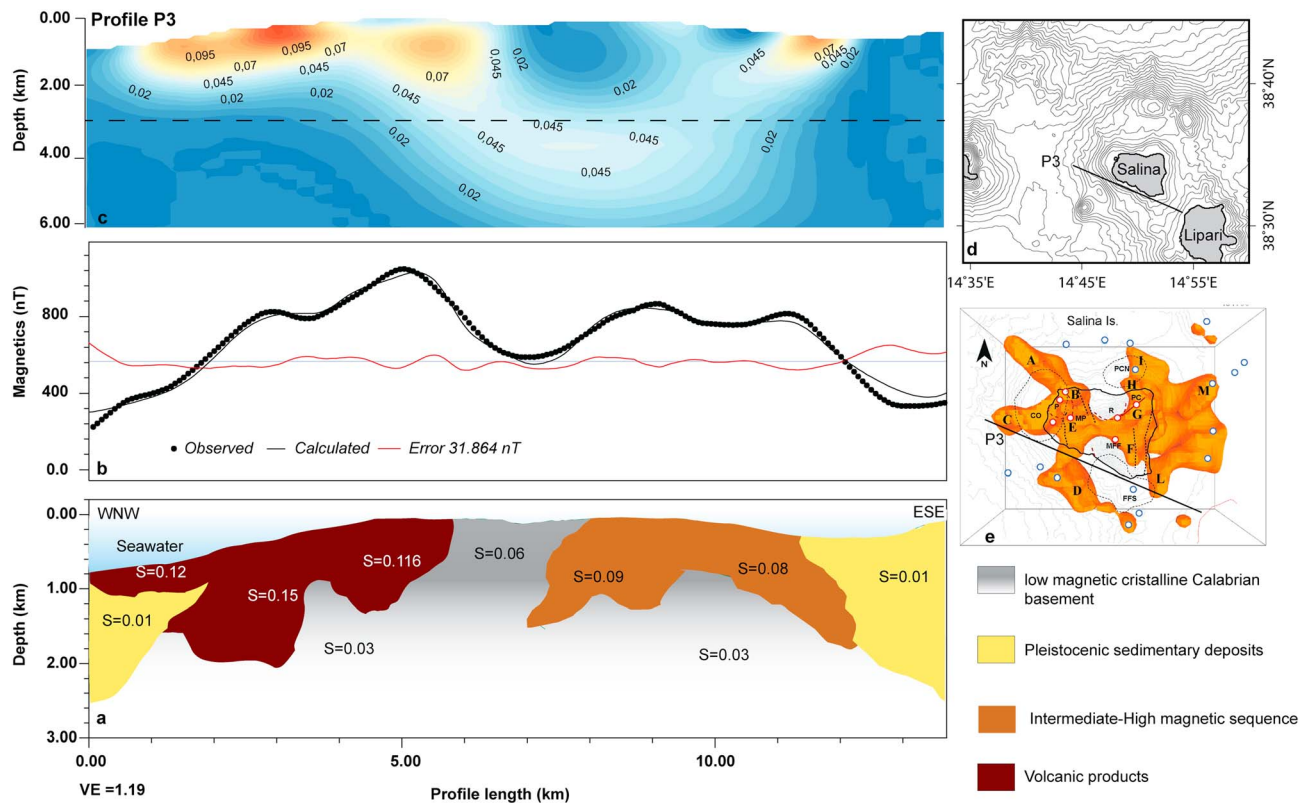
Figure 8. WSW-ENE 2.75-D forward magnetic model of southern off shore area of Salina Island (track of profile P3 in the insets on subpanel d); (a) distribution of magnetized causative bodies obtained by best fit between observed and computed magnetic anomaly profiles (subpanel b). (c) X-Z cross section extracted from 3-D inverse model (Figure 5); the dashed line identifies the depth extension of forward model. (e) The top view of the 3-D inversion of Figure 5.

construction stages of Salina, later on cut by the formation of the large insular shelves developed around the flank of the island.

The morphology of the Pollara horseshoe-shaped depression and the Monte dei Porri western flank suggests a lateral collapse of the Monte dei Porri volcano (Figures 1c and 2; Lucchi, Gertisser, et al., 2013; Lucchi, Tranne, et al., 2013), whose bounding rims roughly follow the trends of the above discussed dyke-like magnetic sources A and C (Figure 5). Therefore, we suggest that these two dyke swarms, which merge below the Monte dei Porri volcano and Pollara crater, have played a role in controlling the geometry of the Monte dei Porri superficial flank collapse. As observed in other volcanic islands, for example, at Reunion Island (Indian Ocean) and Stromboli Island (Aeolian Islands), dykes usually delimit the collapsed sector of volcanoes because they represent higher-strength, subvertical walls delimiting lower-strength pyroclastics and fractures lavas (Apuani et al., 2005; Letourneur et al., 2008). Therefore, if the volcano is subjected to gravity instability or magma overpressure, preexisting dykes may act as stable walls controlling the extent of the gravity or magma-induced deformation. The age of the Monte dei Porri collapse is constrained between the collapsed younger Monte dei Porri lava flows (70-57 ka) and the Punta di Perciato lava flow (30 ka) emplaced after the collapse (Lucchi, Gertisser, et al., 2013). At the eastern tip of the magnetic anomaly A, anomaly B is modeled as a subvertical source, which can be interpreted as the shallower expression of the Pollara crater (30–15 ka) plumbing system. We conclude that the early activity along the dykes evidenced by the seafloor morphology of the western Salina offshore (Figure 1c) and by the underlying corresponding magnetic sources A and C (Figures 5, 6 and 11) started along eruptive fissures, whereas the later activity occurred at the eastern tip of the dykes from a subcircular, shallower conduit. A similar interpretation is here proposed for the dyke-like, NNW-SSE elongated anomaly D (Figures 5 and 8), which is located in correspondence of small-scale submarine eruptive centers in the southwestern offshore of Salina and lava flows occurring at the northwestern tip of the dyke (Figure 1c). Also, in this case, the activity likely started with the emplacement of a
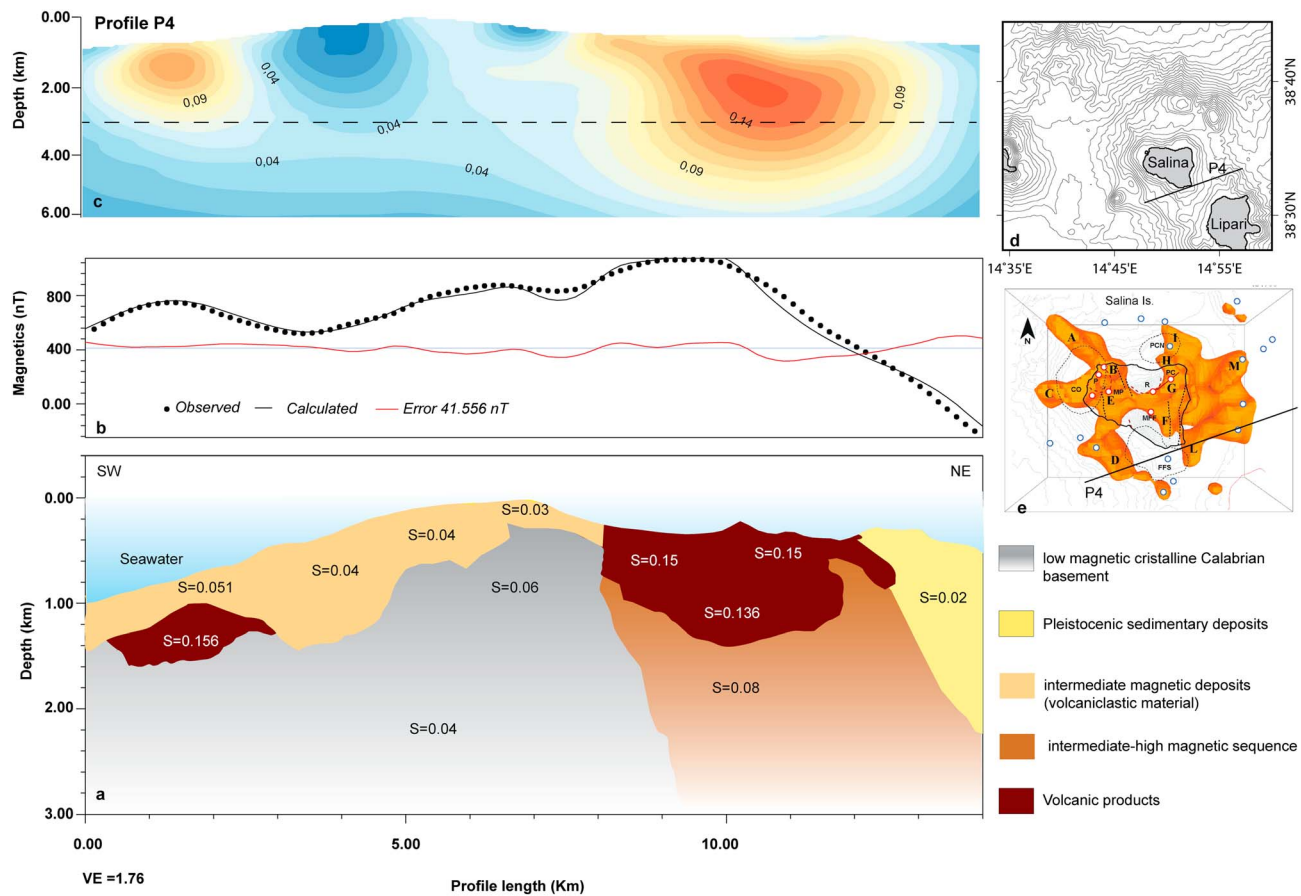
Figure 9. SW-NE 2.75-D forward magnetic model of Fossa delle Felci offshore sector of Salina Island (track of profile P4 in the insets on subpanel d); (a) distribution of magnetized causative bodies obtained by best fit between observed and computed magnetic anomaly profiles (subpanel b). (c) *X-Z* cross section extracted from 3-D inverse model (Figure 5); the dashed line identifies the depth extension of forward model. (e) The top view of the 3-D inversion of Figure 5.

NNW-SSE to NW-SE striking dyke. The strike of the dyke-like magnetic sources A and D is that of the faults affecting the western sector of Salina in the Monte dei Porri area (Figures 2, 3 and 5) and that of the Tindari-Letojanni lithospheric fault system (Figure 1). Because one of these faults also affects the 15-ka-old younger products of the Pollara crater covering the northern flank of Monte dei Porri, we propose that the NW-SE structural discontinuities at Salina represent a major weakness zone of regional significance, along which the dykes of the preisland construction stages emplaced.

In the eastern sector of Salina, the magnetic sources I, H, G, F, and L (Figure 5) align along a N-S strike. This is also the strike of a fault inferred by geomorphological data (Critelli et al., 1993) as affecting the easternmost sector of the island (Figure 2) and the strike of the second-order shears associated to the Tindari-Letojanni lithospheric fault system (De Astis et al., 2003). According with the results from the 3-D inverse and 2.75-D forward models, we infer a relative deepening of the shallower plumbing systems related to the western onshore and offshore Salina volcanoes. A preliminary hypothesis is that such deepening is related to differences in the shallow parts of the plumbing systems directly linked to a variable composition of the products in the western and eastern sectors of Salina, that is, to the prevailing basaltic rocks of the eastern volcanoes (Pizzo del Capo, Monte Rivi, and Monte Fossa delle Felci) with respect to the more evolved andesites to rhyolites of the western one (Monte dei Porri and Pollara; Figure 2). Ganne et al. (2018) show that the crystal mush zones associated to mafic magmas are generally located in deeper positions than those associated to the more evolved ones, which, in addition, tend to ascend to shallower levels because of their lower density. Such observation is consistent with the eastward deepening of the top of the magnetic sources. This interpretation also holds for the onshore, subaerial volcanoes, but it cannot be invoked for the linear, shallower sources affecting the western Salina offshore. Sources I, H, and G overlap the submerged vent
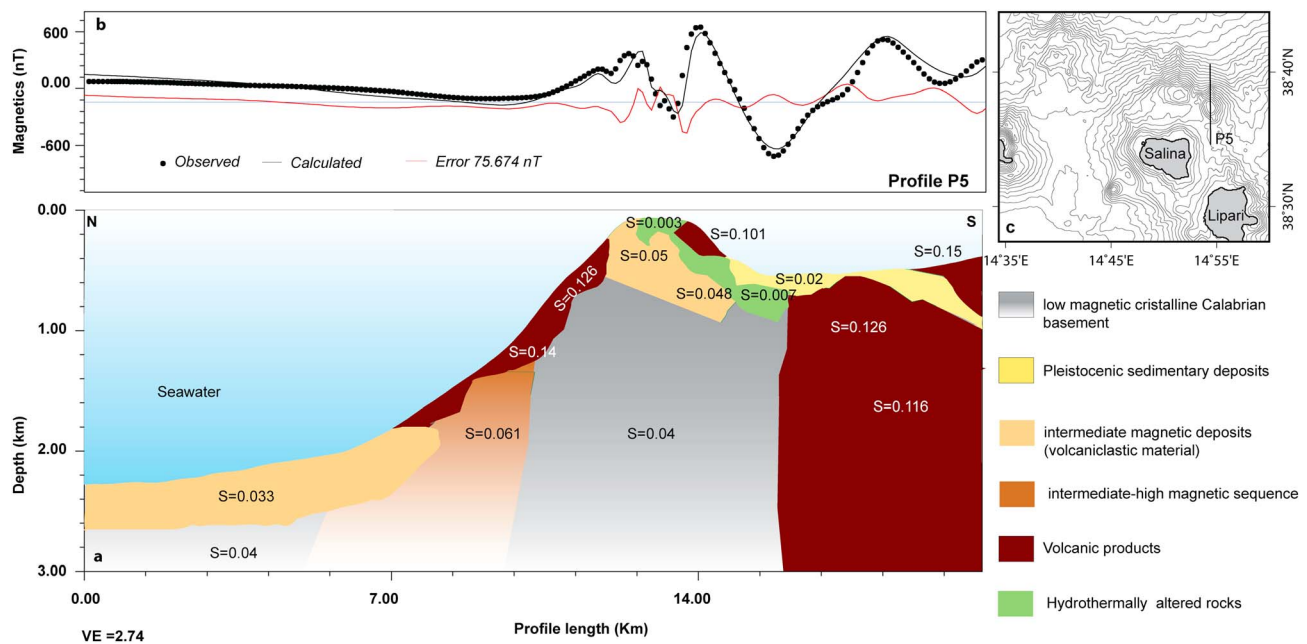
Figure 10. NNW-SSE striking 2.75-D forward magnetic model of southern Secca del Capo area (track of profile P5 in the insets on subpanel c); (a) distribution of magnetized causative bodies obtained by best fit between observed and computed magnetic anomaly profiles (subpanel b).

Figure 11. E-W 2.75-D forward magnetic model of southern entire Salina island and part of the northern Lipari offshore (track of profile P6 in the insets subpanel d); (a) distribution of magnetized causative bodies obtained by best fit between observed and computed mag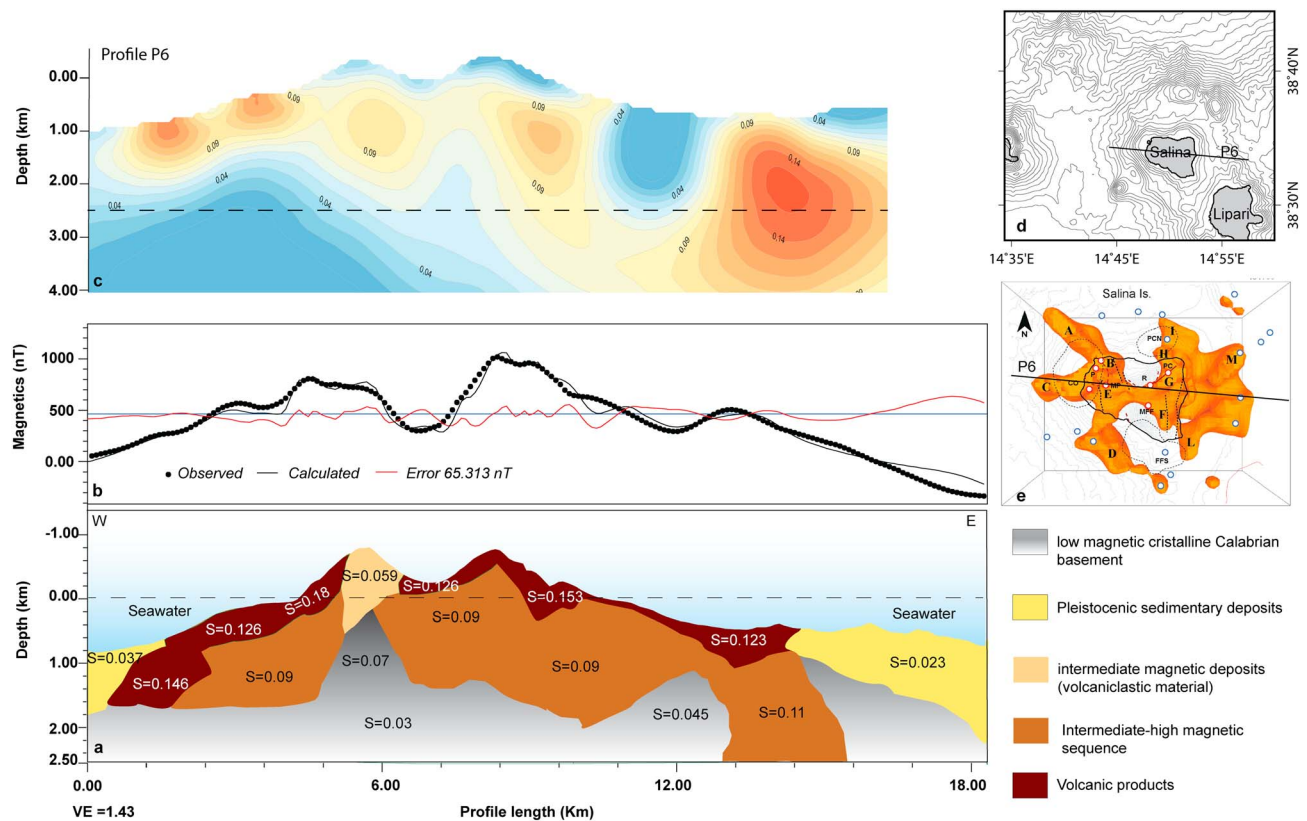netic anomaly profiles (subpanel b). (c) X-Z cross section extracted from 3-D inverse model (Figure 5); the dashed line identifies the depth extension of forward model. (e) The top view of the 3-D inversion of Figure 5.

of Pizzo del Capo North (PCN in Figure 1c; Figure 5) and the onshore vents of the basaltic Pizzo Capo whose products are mostly basalts to basaltic andesites. The eastern boundaries of these sources overlap the rim of the lateral collapse affecting the northern flank of Monte Rivi (Figurers 2 and 5; Lucchi, Gertisser, et al., 2013). The lack of highly magnetized bodies in the collapsed area is related to the removal of volcanic products by the collapse (Figure 5) and/or connected to the presence of chaotic deposits having null remanent susceptibility signature (Speranza et al., 2008). The age of this collapse is uncertain but the occurrence a well-developed shelf offshore the northern flank of Monte Rivi (Figure 1c) and the lack of any debris bulge in the offshore indicate that (a) the collapse episode occurred before the Last Glacial Maximum and/or (b) it affected only the subaerial portion of the volcano. Finally, the easternmost source M (Figure 5) and the less intense and more articulated source of the Secca del Capo seamount (Figure 10) evidences the occurrence of subvertical conduits and submarine lavas of the volcanic field located north of Lipari, and the hydrothermally-altered products of the Secca del Capo area, respectively.

Our results show that the pre-emersion stage of Salina was featured by the emplacement of elongated anomalies related to dykes preferentially located along weakness zones, with strikes similar to those of the main fault systems affecting the central sector of the Aeolian Islands. The western offshore area was characterized by more localized, subcircular and elongated anomalies reflecting the occurrence of now crystallized magmatic bodies, whose location and alignment are also partly controlled by faults. This arrangement mimics that of 'stellate' or rift-like shape of some volcanic islands and seamounts (e.g., El Hierro, Gran Canaria in the Canary islands, Atlantic Ocean, and West Mata seamount, Pacific Ocean; Clague et al., 2011; Karátson et al., 2016; León et al., 2016). However, these stellate shapes are generally associated to (a) landslides particularly favored by the relevant height (>2 km) of the volcanoes and (b) lateral magma migration along a preferential strike, respectively (Mitchell, 2001; Tibaldi, 2015). Differently, the submarine activity of Salina was more complex being characterized by the emplacement of partly intersecting dykes during a preemersion stage and by successive eruptions from small-size, now fully eroded centers formed before 220–248 ka and located along dykes (Figures 1c and 2). The activity occurred only in part along fissures (e.g., the Pizzo di Capo eruptive fissure in Figure 2) and concentrated between 147 and 15 ka in the central, cone-shaped volcanoes of Monte Fossa delle Felci and Monte dei Porri, and in the Pollara crater. Therefore, Salina was characterized by a transition from an early basaltic, fissural activity from intersecting dykes, to a later central activity of more evolved products from central-type volcanoes. The most evolved products (rhyolites) were erupted in the latest phase of activity between 24 and 13 ka. In this phase, all the major central volcanoes, which mainly consist of basalts, basaltic andesites, and minor, later andesites and dacites, were already constructed. The general evolution of Salina indicates the progressive formation, with decreasing time, of shallower reservoirs in which the magma evolved. This evolutive pattern is supported by independent data on fluid inclusions on the xenolithes of the 70 to 57 ka old Monte dei Porri volcano (Lucchi, Gertisser, et al., 2013; Zanon & Nikogosian, 2004). These data evidence a deep reservoir at depth >12.7 km and a shallower storage zone at 1.3- to 2.8-km depth. This latter depth interval is fully coherent with the depths we get for the magnetic source E depicted in Figure 5. This general evolution scheme is consistent with an early formation of weakness zones in the intersection areas of the faults. These intersections allow magma channelization processes, as observed in other volcanoes (e.g., Nisyros Island, Greece, and Vesuvius volcano, Italy; Bianco et al., 1998; Nomikou & Papanikolaou, 2011). Moreover, the progressive growth of the Salina edifice, with the evolution from a seamount to a volcanic island, may also have contributed to focus the initially separated dykes, allowing the convergence of these linear conduits to a restricted area located below the island. Analogue experiments by Muller et al. (2001) and numerical models by Pinel et al. (2017) show that the loading induced by an increasing topography related to the growth of an edifice attracts initially separated dyke-like conduits to converge in a single zone located below the volcano and to reduce the magma ascent velocity, thus promoting the formation of shallow reservoirs in which the magma may evolve. Alternatively, the transition from a fissural to central-type activity in volcanoes is also generally interpreted as related to (a) a re-orientation of the stress within the volcano due to a collapse (Ventura et al., 1999; Walter et al., 2005), (b) increase of magma viscosity at the walls of dykes and successive flow localization along a circular conduit (Wylie et al., 1999), and (c) progressive melting of the country rocks around dykes (Quareni et al., 2001). However, we exclude these other possible mechanisms because collapses tend to divert the ascending magma to the periphery of the new-formed depression, and the flow localization at the

walls of dykes or the melting of the country rocks produces subcircular conduits located in the central portion of the dykes, which has been not observed at Salina, where the major, younger central volcanoes are located at the tip of the early dykes (Figure 5).

6. Conclusions

The results of the magnetic modeling combined with subaerial and offshore geologic evidence indicate that the Salina volcanic complex is characterized by highly magnetized < 3,000-m-deep bodies representing dyke-like intrusions, sheet-like lava flows, and cylindrical conduits. The merging of magnetic and geological data indicate that the Salina area was characterized by a submarine phase mainly controlled by the emplacement of intersecting dykes along which the successive subaerial (most of them presently submerged) volcanoes formed. These dykes, which play a role in controlling the geometry of lateral collapses in the upper part of the volcanic edifice, emplaced along weakness zones with tectonic significance. The dyke intersection zones allow the focusing of magma ascent paths along subvertical, circular conduits. The mechanisms of this transition from a fissural to central-type activity cannot be explained by stress variations due to the formation of large collapse depressions or by flow localization by thermal processes (melting of the whole rock or cooling at the conduit walls). As the Salina edifice growth, the dykes tend to converge below the main edifices, further allowing the formation of shallow reservoir in which magma may evolve. This conceptual model thus explains the magmatic evolution from early basalts to later andesites and rhyolites. In summary, our study highlights how preexisting tectonic structures and progressive loading processes related to the volcano growth may modulate the structural evolution of volcanic islands from an early submarine phase to the emersion stage.

References

Ade-Hall, J. M., Palmer, H. C., & Hubbard, T. P. (1971). The magnetic and opaque petrological response of basalts to regional hydrothermal alteration. *Royal Astronomical Society Geophysics Journal*, *24*(2), 137–174. https://doi.org/10.1111/j.1365-246X.1971.tb02171.x

Apuani, T., Corazzato, C., Cancelli, A., & Tibaldi, A. (2005). Physical and mechanical properties of rock masses at Stromboli: A dataset for flank instability evaluation. *Bulletin of Engineering Geology and the Environment*, *64*(4), 419–431. https://doi.org/10.1007/s10064-005-0007-0

Barberi, F., Gandino, A., Gioncada, A., La Torre, P., Sbrana, A., & Zenucchini, C. (1994). The deep structure of the Eolian arc (Filicudi-Panarea-Vulcano sector) in light of gravity, magnetic and volcanological data. *Journal of Volcanology and Geothermal Research*, *61*(3-4), 189–206. https://doi.org/10.1016/0377-0273(94)90003-5

Barreca, G., Bruno, V., Cultrera, F., Mattia, M., Monaco, C., & Scarfì, L. (2014). New insights in the geodynamics of the Lipari–Vulcano area (Aeolian archipelago, southern Italy) from geological, geodetic and seismological data. *Journal of Geodynamics*, *82*, 150–167. https://doi.org/10.1016/j.jog.2014.07.003

Bianco, F., Castellano, M., Milano, G., Ventura, G., & Vilardo, G. (1998). The Somma-Vesuvius stress field induced by regional tectonics: Evidences from seismological and mesostructural data. *Journal of Volcanology and Geothermal Research*, *82*(1-4), 199–218. https://doi.org/10.1016/S0377-0273(97)00065-6

Billi, A., Barberi, G., Faccenna, C., Neri, G., Pepe, F., & Sulli, A. (2006). Tectonics and seismicity of the Tindari Fault System, southern Italy: Crustal deformations at the transition between ongoing contractional and extensional domains located above the edge of a subducting slab. *Tectonics*, *25*, TC2006. https://doi.org/10.1029/2004TC001763

Blanco-Montenegro, I., De Ritis, R., & Chiappini, M. (2007). Imaging and modelling the subsurface structure of volcanic calderas with high-resolution aeromagnetic data at Vulcano (Aeolian Islands, Italy). *Bulletin of Volcanology*, *69*(6), 643–659. https://doi.org/10.1007/s00445-006-0100-7

Bosman, A., Casalbore, D., Romagnoli, C., & Chiocci, F. L. (2014). Formation of an 'a'ā lava delta: insights from time-lapse multibeam bathymetry and direct observations during the Stromboli 2007 eruption. *Bulletin of Volcanology*, *76*(7), 1–12. https://doi.org/10.1007/s00445-014-0838-2

Calanchi, N., Romagnoli, C., & Rossi, P. L. (1995). Morphostructural features and some petrochemical data from the submerged area around Alicudi and Filicudi volcanic islands (Aeolian Arc, Southern Tyrrhenian Sea). *Marine Geology*, *123*(3-4), 215–238. https://doi.org/10.1016/0025-3227(95)00002-G

Carracedo, J. C. (1994). The Canary Island: An example of structural control on the growth of large oceanic-island volcanoes. *Journal of Volcanology and Geothermal Research*, *60*(3-4), 225–241. https://doi.org/10.1016/0377-0273(94)90053-1

Casalbore, D. (2018). Volcanic islands and seamounts. In A. Micallef, S. Krastel, & A. Savini (Eds.), *Submarine geomorphology* (pp. 333–347). Birkhäuser Verlag AG: Springer Geology.

Casalbore, D., Bosman, A., Romagnoli, C., & Chiocci, F. L. (2016). Morphological map of Salina offshore (Southern Tyrrhenian Sea). *Journal of Maps*, *12*(5), 725–730. https://doi.org/10.1080/17445647.2015.1070300

Clague, D. A., Paduan, J. B., Caress, D. W., Thomas, H., Chadwick, W. W. Jr., & Merle, S. G. (2011). Volcanic morphology of West Mata Volcano, NE Lau Basin, based on high-resolution bathymetry and depth changes. *Geochemistry, Geophysics, Geosystems*, *12*, Q0AF03. https://doi.org/10.1029/2011GC003791

Critelli, S., Sorriso-Valvo, M., & Ventura, G. (1993). Relazioni tra attività vulcanica, sedimentazione epiclastica ed evoluzione geomorfologica nell'Isola di Salina (Isole Eolie). *Bollettino della Societa Geologica Italiana*, *112*, 447–470.

De Astis, G., Ventura, G., & Vilardo, G. (2003). Geodynamic significance of the Aeolian volcanism (Southern Tyrrhenian Sea, Italy) in light of structural, seismological and geochemical data. *Tectonics*, *22*(4), 1040. https://doi.org/10.1029/2003TC001506

De Ritis, R., Ravat, D., Ventura, G., & Chiappini, M. (2013). Curie isotherm depth from aeromagnetic data constraining shallow heat source depths in the central Aeolian Ridge (Southern Tyrrhenian Sea, Italy). *Bulletin of Volcanology*, *75*(4). https://doi.org/10.1007/s00445-013-0710-9

De Ritis, R., Ventura, G., & Chiappini, M. (2007). Aeromagnetic anomalies reveal hidden tectonic and volcanic structures in the central sector of the Aeolian Islands, southern Tyrrhenian Sea, Italy. *Journal of Geophysical Research*, *112*(B10), B10105. https://doi.org/10.1029/2006JB004639

Dialti, L., De Lucia, A., Marziani, F., Niccolini, A., Zeppetella, A., Di Fava, M., et al. (2013). Rapporto sulle attività geofisiche, oceano-grafiche e di campionamento durante la crociera PANSTR12 con Nave Aretusa: Isole Eolie (Stromboli, Panarea, Salina) (2012-06-30-2012-07-14). Rapporti Tecnici INGV, 245, 5-21.

Doglioni, C. (1991). A proposal of kinematic modelling for W-dipping subductions—Possible applications to the Tyrrhenian Apennines system. *Terra Nova*, *3*(4), 423–434. https://doi.org/10.1111/j.1365-3121.1991.tb00172.x

Ferraccioli, F., Gambetta, M., & Bozzo, E. (1998). Microlevelling procedures applied to regional aeromagnetic data: An example from the Transantarctic Mountains (Antarctica). *Geophysical Prospecting*, *46*(2), 177–196. https://doi.org/10.1046/j.1365-2478.1998.00080.x

Gamberi, F., Marani, M., & Savelli, C. (1997). Tectonic, volcanic and hydrothermal features of a submarine portion of the Aeolian arc (Tyrrhenian Sea). *Marine Geology*, *140*(1-2), 167–181. https://doi.org/10.1016/S0025-3227(97)00020-0

Ganne, J., Bachmann, O., & Feng, X. (2018). Deep into magma plumbing systems: Interrogating the crystal cargo of volcanic deposits. *Geology*, *46*(5), 415–418. https://doi.org/10.1130/G39857.1

Gertisser, R., & Keller, J. (2000). From basalt to dacite: Origin and evolution of the calc-alkaline series of Salina, Aeolian Arc, Italy. *Contributions to Mineralogy and Petrology*, *139*(5), 607–626. https://doi.org/10.1007/s004100000159

Grosse, P., van Wyk de Vries, B., Euillades, P. A., & Euillades, L. D. (2014). A global database of composite volcano morphometry. *Bulletin of Volcanology*, *76*(1), 1–16. https://doi.org/10.1007/s00445-013-0784-4

Gudmundsson, A. (1998). Magma chambers modeled as cavities explain the formation of rift zone central volcanoes and their eruption and intrusion statistics. *Journal of Geophysical Research*, *103*(B4), 7401–7412. https://doi.org/10.1029/97JB03747

Gvirtzman, Z., & Nur, A. (2001). Residual topography, lithospheric thickness, and sunken slabs in the central Mediterranean. *Earth and Planetary Science Letters*, *187*(1-2), 117–130. https://doi.org/10.1016/S0012-821X(01)00272-2

Hinze, W. J., von Frese, R. R. B., & Saad A, H. (2013). Gravity and Magnetic Exploration, Principles, Practices, and Applications. Cambridge, United Kingdom: Cambridge University Press.

Karátson, D., Yepes, J., Favalli, M., Rodríguez-Peces, M. J., & Fornaciai, A. (2016). Reconstructing eroded paleovolcanoes on Gran Canaria, Canary Islands, using advanced geomorphometry. *Geomorphology*, *253*, 123–134. https://doi.org/10.1016/j.geomorph.2015.10.004

Keller, J. (1980). The island of Salina. *Rendiconti della Societa Italiana di Mineralogia e Petrologia*, *36*, 489–524.

Lanza, R., & Zanella, E. (2003). Paleomagnetic secular variation at Vulcano (Aeolian Islands) during the last 135 kyr. *Earth and Planetary Science Letters*, *213*(3-4), 321–336. https://doi.org/10.1016/S0012-821X(03)00326-1

Lanzafame, G., & Bousquet, J. C. (1997). The Maltese escarpment and its extension from Mt. Etna to Aeolian Islands Sicily: Importance and evolution of a lithospheric discontinuity. *Acta Vulcanologica*, *9*, 121–135.

León, R., Somoza, L., Urgeles, R., Medialdea, T., Ferrer, M., Biain, A., et al. (2016). Multi-event oceanic island landslides: New onshore-offshore insights from El Hierro Island, Canary Archipelago. *Marine Geology*, *393*, 156–175. https://doi.org/10.1016/j.margeo.2016.07.001

Letourneur, L., Peltier, A., Staudacher, T., & Gudmundsson, A. (2008). The effects of rock heterogeneities on dyke paths and asymmetric ground deformation: The example of Piton de la Fournaise (Réunion Island). *Journal of Volcanology and Geothermal Research*, *173*(3-4), 289–302. https://doi.org/10.1016/j.jvolgeores.2008.01.018

Li, Y., & Oldenburg, D. W. (1996). 3-D Inversion of magnetic data. *Geophysics*, *61*(2), 394–408. https://doi.org/10.1190/1.1443968

Li, Y., & Oldenburg, D. W. (2003). Fast inversion of large-scale magnetic data using wavelet transforms and a logarithmic barrier method. *Geophysical Journal International*, *152*(2), 251–265. https://doi.org/10.1046/j.1365-246X.2003.01766.x

Lucchi, F., Gertisser, R., Keller, J., Forni, F., De Astis, G., & Tranne, C. A. (2013). Eruptive history and magmatic evolution of the island of Salina (central Aeolian archipelago). In F. Lucchi, A. Peccerillo, J. Keller, C. A. Tranne, & P. L. Rossi (Eds.), *The Aeolian Islands Volcanoes*, *Memoirs*, (Vol. 37, pp. 155–211). London: Geological Society.

Lucchi, F., Tranne, C. A., Keller, J., Gertisser, R., Forni, F., & De Astis, G. (2013). Geological map of the island of Salina, scale 1:10 000 (Aeolian archipelago). In F. Lucchi, A. Peccerillo, J. Keller, C. A. Tranne, & P. L. Rossi (Eds.), *The Aeolian Islands Volcanoes*, *Memoirs*, (Vol. 37, Chap. 9. online material). London: Geological Society. enclosed DVD. https://dx.doi.org/10.6084/m9.figshare.c.2166762

Maccaferri, F., Richter, N., & Walter, T. R. (2017). The effect of giant lateral collapses on magma pathways and the location of volcanism. *Nature Communications*, *8*(1), 1097. https://doi.org/10.1038/s41467-017-01256-2

McClinton, J. T., & White, S. M. (2015). Emplacement of submarine lava flow fields: a geomorphological model from the Niños eruption at the Galapagos Spreading Center. *Geochemistry, Geophysics, Geosystems*, *16*, 899–911. https://doi.org/10.1002/2014GC005632

McGuire, W. (2006). Lateral collapse and tsunamigenic potential of marine volcanoes. In C. Troise, G. De Natale, & C. R. J. Kilburn (Eds.), *Mechanisms of activity and unrest at large calderas*, *Special Publication* (Vol. 269, pp. 121–140). London: Geological Society.

MGinv3D (2013). Scientific Computing and Applications, retrieved from http://www.scicomap.com/MGinv3D.htm.

Mitchell, N. C. (2001). Transition from circular to stellate forms of submarine volcanoes. *Journal of Geophysical Research*, *106*(B2), 1987–2003. https://doi.org/10.1029/2000JB900263

Mitchell, N. C., Beir, C., Rosin, P. L., Quartau, R., & Tempera, F. (2008). Lava penetrating water: submarine lava flows around the coasts of Pico Island Azores. *Geochemistry, Geophysics, Geosystems*, *9*, Q03024. https://doi.org/10.1029/2007GC001725

Muller, J. R., Ito, G., & Martel, S. J. (2001). Effects of volcano loading on dike propagation in an elastic half-space. *Journal of Geophysical Research*, *106*(B6), 11,101–11,113. https://doi.org/10.1029/2000JB900461

Nomikou, P., & Papanikolaou, D. (2011). Extension of active fault zones on Nisyros volcano across the Yali-Nisyros Channel based on onshore and offshore data. *Marine Geophysical Research*, *32*(1-2), 181–192. https://doi.org/10.1007/s11001-011-9119-z

Novosel, I., Spence, G. D., & Hyndman, R. D. (2005). Reduced magnetization produced by increased methan flux at gas hydrate vent. *Marine Geology*, *216*(4), 265–274. https://doi.org/10.1016/j.margeo.2005.02.027

Paine, J., Haederle, M., & Flis, M. (2001). Using Transformed TMI Data to Invert for Remanently Magnetised Bodies. *Exploration Geophysics*, *32*(3–4), 238–242. https://doi.org/10.1071/eg01238

Panieri, G., Gamberi, F., Marani, M., & Barbieri, R. (2005). Benthic foraminifera from a recent, shallow-water hydrothermal environment in the Aeolian Arc (Tyrrhenian Sea). *Marine Geology*, *218*(1–4), 207–229. https://doi.org/10.1016/j.margeo.2005.04.002

Pinel, V., Carrara, A., Maccaferri, F., Rivalta, E., & Corbi, F. (2017). A two-step model for dynamical dike propagation in two dimensions: Application to the July 2001 Etna eruption. *Journal of Geophysical Research: Solid Earth*, *122*, 1107–1125. https://doi.org/10.1002/2016JB013630

Quareni, F., Ventura, G., & Mulargia, F. (2001). Numerical modelling of transitions from fissural to central type activity on volcanoes: A case study from Salina Island, Italy. *Physics of the Earth and Planetary Interiors*, *124*(3-4), 213–221. https://doi.org/10.1016/S0031-9201(01)00197-2

Romagnoli, C. (2013). Characteristics and morphological evolution of the Aeolian volcanoes from the study of submarine portions. In F. Lucchi, A. Peccerillo, J. Keller, C. A. Tranne, & P. L. Rossi (Eds.), *The Aeolian Islands Volcanoes*, *Memoirs* (Vol. 37, pp. 13–26). London: Geological Society.

Romagnoli, C., Calanchi, N., Gabbianelli, G., Lanzafame, G., Rossi, P.L. (1989). Contributi delle ricerche di geologia marina alla caratterizzazione morfostrutturale ed evolutiva dei complessi vulcanici di Salina, Lipari e Vulcano (Is. Eolie). Bollettino GNV-CNR, 1989-2, 971-978.

Romagnoli, C., Casalbore, D., Bortoluzzi, G., Bosman, A., Chiocci, F. L., D'Oriano, F., et al. (2013). Bathy-morphological setting of the Aeolian islands. In F. Lucchi, A. Peccerillo, J. Keller, C. A. Tranne, & P. L. Rossi (Eds.), *The Aeolian Islands Volcanoes*, Memoirs (Vol. *37*, pp. 27–36). London: Geological Society.

Romagnoli, C., Casalbore, D., Ricchi, A., Lucchi, F., Quartau, R., Bosman, A., et al. (2018). Morpho-bathymetric and seismo-stratigraphic analysis of the insular shelf of Salina (Aeolian archipelago) to unveil its Late-Quaternary geological evolution. *Marine Geology*, *395*, 133–151. https://doi.org/10.1016/j.margeo.2017.10.003

Roman, A., & Jaupart, C. (2014). The impact of a volcanic edifice on intrusive and eruptive 776 activity. *Earth and Planetary Science Letters*, *408*, 1–8. https://doi.org/10.1016/j.epsl.2014.09.016

Rona, P. (1978). Magnetic signatures of hydrothermal alteration and volcanogenic mineral deposits in oceanic crust. *Journal of Volcanology and Geothermal Research*, *3*(1-2), 219–225. https://doi.org/10.1016/0377-0273(78)90010-0

Rosenbaum, G., & Lister, G. S. (2004). Neogene and quaternary rollback evolution of the Tyrrhenian Sea, the Apennines, and the Sicilian Maghrebides. *Tectonics*, *23*, TC001397. https://doi.org/10.1029/2003TC001518

Savelli, C. (2000). Two-stage progression of volcanism 8–0 Ma in the central Mediterranean southern Italy. *Journal of Geodynamics*, *31*(4), 393–410. https://doi.org/10.1016/S0264-3707(01)00010-2

Speranza, F., Pompilio, M., D'Ajello Caracciolo, F., & Sagnotti, L. (2008). Holocene eruptive history of the Stromboli volcano: Constraints from paleomagnetic dating. *Journal of Geophysical Research*, *113*(B9), B09101. https://doi.org/10.1029/2007JB005139

Szitkar, F., Petersen, S., Caratori Tontini, F., & Cocchi, L. (2015). High-resolution magnetics reveal the deepstructure of a volcanic-arc-related basalt-hosted hydrothermal site (Palinuro, Tyrrhenian Sea). *Geochemistry, Geophysics, Geosystems*, *16*(6), 1950–1961. https://doi.org/10.1002/2015gc005769

Takada, A. (1989). Magma transport and reservoir formation by a system of propagating cracks. *Bulletin of Volcanology*, *52*(2), 118–126. https://doi.org/10.1007/BF00301551

Thouret, J. C. (1999). Volcanic geomorphology—An overview. *Earth-Science Reviews*, *47*(1-2), 95–131. https://doi.org/10.1016/S0012-8252(99)00014-8

Tibaldi, A. (2015). Structure of volcano plumbing systems: A review of multi-parametric effects. *Journal of Volcanology and Geothermal Research*, *298*, 85–135. https://doi.org/10.1016/j.jvolgeores.2015.03.023

Ventura, G., Vilardo, G., & Bruno, P. P. (1999). The role of flank failure in modifying the shallow plumbing system of volcanoes: An example from Somma–Vesuvius, Italy. *Geophysical Research Letters*, *26*(24), 3681–3684. https://doi.org/10.1029/1999GL005404

Walter, T. R., Troll, V. R., Cailleau, B., Belousov, A., Schmincke, H.-U., Amelung, F., & Bogaard, P. (2005). Rift zone reorganization through flank instability in ocean Island volcanoes: An example from Tenerife,Canary Islands. *Bulletin of Volcanology*, *67*(4), 281–291. https://doi.org/10.1007/s00445-004-0352-z

Won, I. J., & Bevis, M. (1987). Computing the gravitational and magneticanomalies due to a polygon: Algorithms and FORTRAN subroutines. *Geophysics*, *52*, 232–238.

Wylie, J. J., Helfrich, K. R., Dade, B., Lister, J. R., & Salzig, J. F. (1999). Flow localisation in fissure eruptions. *Bulletin of Volcanology*, *60*(6), 432–440. https://doi.org/10.1007/s004450050243

Zanella, E. (1995). Studio delle variazioni paleosecolari del campo magne- tico terrestre registrate nelle vulcaniti Quaternarie dell'area tirrenica e del Canale di Sicila. Ph.D. thesis, 198 pp., Univ. di Torino, Torino, Italy.

Zanon, V., & Nikogosian, I. K. (2004). Evidence of crustal melting events below the Island of Salina (Aeolian Arc, Southern Italy). *Geological Magazine*, *141*(4), 525–540. https://doi.org/10.1017/S0016756804009124

Zhu, C., Byrd, R.H., Lu, P. & Nocedal, J. (1994). L-BFGS-B: a limited memory FORTRAN code for solving bound constrained optimization problems. *Technical Report*, NAM-11, EECS Department, Northwestern University, retrieved from http://users.iems.northwestern.edu/~nocedal/PDFfiles/lbfgsb.pdf